Article

A radiation transfer model for the Milky-Way: I. Radiation fields and application to High Energy Astrophysics

Popescu, Cristina, Yang, R, Tuffs, R J, Natale, Giovanni, Rushton, M and Aharonian, F

Popescu, Cristina ORCID: 0000-0002-7866-702X, Yang, R, Tuffs, R J, Natale, Giovanni, Rushton, M and Aharonian, F (2017) A radiation transfer model for the Milky-Way: I. Radiation fields and application to High Energy Astrophysics. Monthly Notices of the Royal Astronomical Society, 470 (3). pp. 2539-2558. ISSN 0035-8711

Monthly Notices
of the
ROYAL ASTRONOMICAL SOCIETY

MNRAS **470,** 2539–2558 (2017)
Advance Access publication 2017 May 24

doi:10.1093/mnras/stx1282

A radiation transfer model for the Milky Way: I. Radiation fields and application to high-energy astrophysics⋆

C. C. Popescu,[1,2,3]† R. Yang,[3,4] R. J. Tuffs,[3]† G. Natale,[1] M. Rushton[2] and F. Aharonian[3,5]

[1] *Jeremiah Horrocks Institute, University of Central Lancashire, PR1 2HE Preston, UK*
[2] *The Astronomical Institute of the Romanian Academy, Str. Cutitul de Argint 5, Bucharest, Romania*
[3] *Max Planck Institut für Kernphysik, Saupfercheckweg 1, D-69117 Heidelberg, Germany*
[4] *Key Laboratory of Dark Matter and Space Astronomy, Purple Mountain Observatory, Chinese Academy of Sciences, Nanjing 210008, China*
[5] *School of Cosmic Physics, Dublin Institute for Advanced Studies, 31 Fitzwilliam Place, Dublin 2, Ireland*

Accepted 2017 May 22. Received 2017 May 22; in original form 2016 September 19

ABSTRACT

We present a solution for the ultraviolet – submillimetre (submm) interstellar radiation fields (ISRFs) of the Milky Way (MW), derived from modelling *COBE*, *IRAS* and *Planck* maps of the all-sky emission in the near-, mid-, far-infrared and submm. The analysis uses the axisymmetric radiative transfer model that we have previously implemented to model the panchromatic spectral energy distributions (SEDs) of star-forming galaxies in the nearby universe, but with a new methodology allowing for optimization of the radial and vertical geometry of stellar emissivity and dust opacity, as deduced from the highly resolved emission seen from the vantage point of the Sun. As such, this is the first self-consistent model of the broad-band continuum emission from the MW. In this paper, we present model predictions for the spatially integrated SED of the MW as seen from the Sun, showing good agreement with the data, and give a detailed description of the solutions for the distribution of ISRFs, as well as their physical origin, throughout the volume of the galaxy. We explore how the spatial and spectral distributions of our new predictions for the ISRF in the MW affects the amplitude and spectral distributions of the gamma rays produced via inverse Compton scattering for cosmic ray (CR) electrons situated at different positions in the galaxy, as well as the attenuation of the gamma rays due to interactions of the gamma-ray photons with photons of the ISRF. We also compare and contrast our solutions for the ISRF with those incorporated in the GALPROP package used for modelling the high-energy emission from CR in the MW.

Key words: radiation mechanisms: non-thermal – radiative transfer – scattering – cosmic rays – dust, extinction – gamma-rays: ISM.

1 INTRODUCTION

Cosmic rays (CR) are a major energetic constituent of the interstellar medium (ISM) of the Milky Way (MW) and other galaxies, contributing a comparable energy density to that in photons, magnetic field and thermal gas. They control key processes governing galactic evolution both on large scales, such as powering galactic winds, and on small scales, such as in dense star-forming cores of molecular clouds, where they are the dominant ionizing agent enabling magnetic pressure support of the cores. Despite this, the questions of what the global distribution of CRs is within the galaxy, where they originate, and how they propagate in the ISM, are still open. One fundamental reason for these uncertainties is that the solar neighbourhood is still the only place in the Galaxy where we have a truly unambiguous measurement of the amplitude and spectrum of the flux of CR protons and electrons. At any other position, CRs are usually detected via proxies, through gamma-ray emission in the MeV to TeV spectral range, which has two major components: (i) gamma rays arising from the decay of pions produced in the interaction of CR protons and nucleons with interstellar neutral and molecular hydrogen (the hadronic component); (ii) gamma rays arising from the inverse Compton (IC) scattering by CR electrons[1] and positrons of photons in the cosmic

⋆ The data are available in electronic form at the CDS via anonymous ftp to cdsarc.u-strasbg.fr or via http://cdsweb.u-strasbg.fr/cgi-bin/qcat?J/MNRAS/.

† E-mail: cpopescu@uclan.ac.uk (CCP); Richard.Tuffs@mpi-hd.mpg.de (RJT)

[1] CR electrons in the ISM can also be detected in gamma rays via relativistic bremsstrahlung emission, and at radio wavelengths through synchrotron radiation

microwave background (CMB) radiation field (RF) and the interstellar radiation fields (ISRF, the leptonic component). Because the contribution from these two main competing mechanisms is in many cases comparable and their spectral shape not markedly dissimilar (Aharonian & Atoyan 2000), extracting robust information on CR fluxes based on the overall level of gamma-ray emission and on its spectral shape has proven to be difficult. Therefore, additional constraints need to be considered, in particular through prior knowledge of gas column in the case of pion decay, and of ISRFs in the case of the IC effect. While RFs from the CMB are important in providing seed photons for the very energetic TeV gamma-ray photons, it is the 10–1000 μm mid-infrared (MIR), far-infrared (FIR) and submillimetre (submm) RFs, originating from dust emission, that provide the seed photons for an important part of the gamma-ray spectrum in the GeV–TeV range, and the 0.1–10 μm ultraviolet (UV), optical and near-infrared (NIR) RFs originating from stellar sources that power the MeV gamma-ray emission. In addition, the infrared RFs affect the propagation of gamma rays through the intergalactic and ISM (Moskalenko, Porter & Strong 2006) through pair production of gamma-ray photons on the background RFs.

That there has been relatively little focus on the quantification of ISRFs in galaxies in general, and in the MW in particular, may be due to the fact that they are not directly measurable and thus difficult to determine. It would be relatively straightforward to determine RFs by direct observations of the sources of photons, which, in most cases, are predominantly stars, if galaxies were optically thin. However, galaxies – and in particular star-forming galaxies – contain dust grains, which, because they absorb and scatter photons, partially or wholly prevent a direct measurement of the spatial and spectral distribution of the sources of the RFs in the UV/optical. The propagation of light depends in a complex way on the relative distribution of stellar emissivity and dust opacity, with structures ranging in scale from parsecs to kiloparsecs. However, the stellar light that is absorbed by dust is re-radiated in the IR/submm range, with spectral characteristics directly related to the heating by stellar RFs. Thus, images of the amplitude and colour of the IR/submm emission can potentially place strong constraints on the distribution of the UV/optical ISRF within galaxies, even when stellar populations are obscured. Moreover, if, as is almost always the case, galaxies are optically thin in the FIR/submm, observed images can provide a more direct constraint on the spatial distribution of the emissivity, and thereby the ISRF, in these bands.

Work on modelling external galaxies observed in the IR/submm has confirmed that radiative transfer techniques can be used to self-consistently link the RFs to the spectral energy distributions (SEDs) in the UV/optical/IR/submm, in combination with independent empirical constraints on the spatial distribution of young and old stellar populations and of dust (Popescu et al. 2000a; Misiriotis et al. 2001; Popescu et al. 2004; Bianchi 2007; Baes et al. 2010; Bianchi & Xilouris 2011; MacLachlan et al. 2011; De Looze et al. 2012a, b; 2014).

Since the MW is the best observed galaxy, and our nearest astrophysical laboratory, it is clearly desirable to extend the self-consistent radiative transfer (RT) analysis of the panchromatic emission of external spiral galaxies to determine the UV/optical/IR/submm RFs throughout the volume of the ISM of our own galaxy. Here, we present results of such an analysis, obtained using a development of the axisymmetric RT model that we have previously implemented to model the integrated panchromatic SEDs of nearby spiral galaxies (Popescu et al. 2000a; Tuffs et al. 2004; Popescu et al. 2011, referred to as PT11 in this paper). This model has been successful in accounting for both the spatially integrated SEDs of individual galaxies (Popescu et al. 2000a, Misiriotis et al. 2001) and to predict the appearance of the modelled galaxies in the dust emission (Popescu et al. 2004; Popescu et al. 2011). Generic solutions for the distribution of ISRF in external galaxies implicit to the model SEDs presented in PT11 are given in Popescu & Tuffs (2013). The PT11 model has also predicted the statistical behaviour of a variety of observables of the population of spiral galaxies in the local Universe (Driver et al. 2007, 2008, 2012; Graham & Worley 2008; Masters et al. 2010; Gunawardhana et al. 2011; Kelvin et al. 2012, 2014; Grootes et al. 2013a; Pastrav et al. 2013a, b; Vulcani et al. 2014; Devour & Bell 2016). Grootes et al. (2013b) has shown that using the RT model of PT11 to correct the fundamental scaling relation between specific star formation rates (SFRs), as measured from the UV continuum, and stellar mass for the effects of dust attenuation leads to a marked reduction of the scatter in this relation, confirming the ability of the PT11 model to predict the propagation of UV light in galaxies. Recently, Davies et al. (2016) has shown that, when critically compared and contrasted with various methods to derive SFRs in galaxies, the one using this RT method gives the most consistent slopes and normalizations of the specific SFR–stellar mass relations.

Previous studies of the large-scale distribution of stars and diffuse dust emission in the MW have often separately modelled either star count data or the dust emission, without linking the two by a RT calculation to explicitly predict the IR/submm emission of grains in response to the ISRF at each position in the galaxy. Stellar distribution models include the Besançon model (Robin & Creze 1986; Bienayme, Robin & Creze 1987; Robin et al. 1996, 2003), the SKY model (Wainscoat et al. 1992; Cohen 1993, 1994, 1995) and the TRILEGAL model (Girardi et al. 2005). Models of the diffuse dust emission in the MW have also been developed to reproduce the large-scale MIR and FIR emission: Sodroski et al. (1997), Davies et al. (1997), Drimmel (2000), Drimmel & Spergel (2001) and Misiriotis et al. (2006). In the cases that self-consistent RT models have been employed, these have been used to only model a very limited wavelength and spatial range, or have not been optimized to fit all-sky emission observational data. Thus, Robitaille et al. (2012) developed a non-axisymmetric RT model of the MW which was only compared to the MIR data and only for 274 deg^2; because only a very narrow strip in latitude was used for comparison purposes, no handle on the contamination from highly resolved foreground emission from structures local to the Sun could have been applied. In addition, the model does not incorporate local absorption and emission in the star-forming regions, which are the main contributors to the MIR emission in star-forming galaxies in the 25 and 60 μm bands. Another RT model is that incorporated in the GALPROP package, developed and continuously improved in the last 16 yr (Strong, Moskalenko & Reimer 2000; Moskalenko et al. 2002; Porter et al. 2006; Moskalenko et al. 2006; Porter et al. 2008). This is an axisymmetric model providing an explicit calculation of the RFs in the MW, which was specifically designed for use in studies of the high-energy gamma-ray emission. However, this model was not optimized to fit the all-sky observational data in the NIR–FIR–submm, but was built using the assumption that the stellar and dust distributions are known from stellar counts and gas measurements. As with the Robitaille model, the GALPROP model does not incorporate the contribution of star-forming regions, and was recently shown to not predict the observed *IRAS*, *COBE* and *Planck* maps of the MW (Porter 2016).

In this context, it is to be noted that modelling the panchromatic emission from the MW is in practice a far more challenging

problem than for external galaxies. This is in large measure due to the position of the Sun within the galaxy, which induces a massive degeneracy, not present in the extragalactic studies, between the distance to the observer and the luminosity of emitters. This difficulty is compounded by the fact that, from the vantage point of the Sun, dust in the galactic plane obscures almost all direct stellar light from the inner galaxy shortwards of 3 μm; by contrast, even in an edge-on view, visual measurements can still be used to constrain the RT analysis of external spiral galaxies. The luminosity–distance degeneracy may potentially be sidestepped by assuming some physical link between dust grains and gas in galaxies, since radio spectroscopic observations of gas tracers (primarily the hyperfine 21 cm hydrogen line to trace H I and rotational transitions of the CO molecule to trace H_2) can be used to model the distribution of the gas. Indeed, this approach has been commonly adopted in modelling imaging observations of the dust emission, including the RT analyses of Porter et al. (2008) and Robitaille et al. (2012). However, the transformations between the radio tracers and the actual distribution of the gas are themselves challenging to physically model and are empirically uncertain. This, in turn, may potentially introduce systematic error into the model predictions for the ISRF. Moreover (and motivated by the empirical uncertainty in the conversion factors of the radio tracers), one fundamental goal of modelling the gamma-ray emission from the MW will ultimately be to use the pion-decay component of the emission to determine the hydrogen gas distribution in the MW completely independently of the radio tracers; for such an analysis one would also require that the predictions of the IC component of the gamma-ray emission be independent of the radio tracers.

Motivated by these considerations, the observational input for our RT model for the panchromatic emission from the MW is restricted to the distributions of surface brightness of the galaxy provided by the *COBE*, *IRAS* and *Planck* maps of the all-sky emission in the NIR, MIR, FIR and submm. In a separate paper (Natale et al., in preparation), we describe in detail the modifications to the methodology of the PT11 model to allow the radial and vertical distributions of stellar emissivity and dust opacity to be deduced from the highly resolved emission maps. In this approach, we are in effect using an assumption of axisymmetry to break the luminosity–distance degeneracy, and related degeneracies affecting the radial distributions of dust and stellar emissivity.

In this paper, we present the model predictions for the corresponding solutions for the spatial and spectral dependencies of the solutions for the ISRFs from the UV to the submm. We also make these solutions available in electronic format for use in the analysis of gamma-ray emission in our Galaxy. These should help interpret the broad range of gamma-ray observations that have been recently carried with the *Fermi* Gamma-ray Space Telescope in the energy range from 100 MeV to 300 GeV and with the High Energy Stereoscopic System (HESS) ground-based Cherenkov telescope at the high-energy end in the range from 0.1 to 10 TeV. This will constrain the interpretation of the large-scale diffuse gamma-ray emission of the MW, in effect by imposing consistency between the IC component of the gamma-ray emission and the completely independent NIR–submm data on direct and dust-re-radiated starlight. It will also constrain the interpretation of discrete gamma-ray sources embedded in the diffuse ISM, such as plerions, shell-type SNRs, binary systems, or other as yet unidentified sources of gamma rays.

The structure of the paper is as follows: In Section 2, we give an overview of the RT model used for the calculations of the RFs in the MW. In Section 3, we show the predictions of our model for the dust emission SED of the MW and compare this with the observed spatially integrated SED derived from *IRAS*, *COBE* and *Planck* maps. We also show predictions for the local ISRF extending into the UV/optical regime and compare this with observational constraints on the local UV/optical ISRF. The results of our model are described in terms of radial and vertical profiles and SEDs of RFs in Section 4. The resulting RFs presented in this paper are compared with those predicted by the GALPROP model in Section 5. In Section 6, we explore how the spatial and spectral distributions of the ISRF affects the spatial and spectral distributions of the gamma rays produced via IC scattering, as well as the attenuation of the gamma rays due to interactions of the gamma-ray photons with photons of the ISRF. In Section 7, we discuss the influence of the modelled ISRF on predicted very high energy (VHE) emission from accelerators of CR electrons. In Section 8, we give a summary of our main results.

2 THE MODEL

Our model is based on the axisymmetric RT model of PT11 for the UV to submm emission of external galaxies, in which the geometry of dust opacity and stellar emissivity is prescribed by parametrized functional forms. In the PT11 model, values of all geometric parameters had fixed ratios to the scalelength of an exponential disc describing stellar emissivity in the *B* band, with the ratios being calibrated either from resolved observations of translucent components of edge-on spiral galaxies exhibiting dust lanes (Xilouris et al. 1999), or, for highly obscured structure associated with young stellar populations, set according to physical considerations, and such that the observed amplitude and spectrum of the observed integrated IR emission from dust could be predicted. A key ingredient of the model for external galaxies, which we also found necessary to reproduce the observed images of the MW in both direct and dust-re-radiated starlight, is the use of separate discs to describe the emissivities of the young and old stellar populations, with the latter having a larger scaleheight than the former. As for the external galaxies, we also needed to invoke separate geometrically thin and thick dust discs to be respectively associated with the discs of young and old stellar emissivity in the MW.

While retaining the overall formalism of the PT11 model as applied to the MW, we nevertheless had to implement a new methodology that deals with the inner view of a galaxy and with the lack of direct observational constraints in the UV–optical regime within the solar circle. We thus optimized the geometrical components of the model and the value of the model parameters to fit the observed maps seen from the position of the Sun in the submm, FIR and NIR. The description of this detailed modelling is given in Natale et al. (in preparation) . Here, we only mention its main characteristics that are relevant for the understanding of the solution for the RFs. The main concept in the optimization procedure is that we made use of the fact that each waveband is strongly affected only by a subset of parameters. For example, the observed latitude and longitude profiles in the submm provided strong constraints for the radial and vertical distributions of diffuse dust. The distribution of 24 μm emission constrained the distribution of locally obscured star-forming regions, while the NIR emission was used to derive the characteristics of the old stellar populations, including their optical emission. The maps at the peak of the dust emission SED were important in deriving the distribution of diffuse UV heating, otherwise not directly accessible to observations. Therefore, we were able to compartmentalize the optimization problem and introduce a hierarchy into this which avoided the need to simultaneously solve for all geometrical parameters. After solving for each subdomain

in the hierarchy of parameters, we revisited the other domains to ensure a fully self-consistent calculation over all parameters. Several cycles over this hierarchy were needed to converge on the final solution. In each case, the best-fitting model was determined by visually comparing the predicted brightness profiles in longitude averaged over latitude, and in latitude averaged over longitude with the corresponding observed brightness profiles. When needed (in particular to verify the model prescription for the variation of scale-height with radius), a comparison was also made between model and data for strip latitude profiles at various longitudes. In the context of the applications to gamma-ray astronomy, we found that the predicted amplitudes of the IR component of the ISRF, which is the most important for predicting IC emission from CR electrons, were especially sensitive to the vertical scale of the dust distribution.

The result of this new optimization technique led to a solution for the distribution of dust and stars that were able to self-consistently reproduce the overall average latitude and longitude profiles derived from the *COBE* maps at 1.2, 2.2, 3.5, 4.6, 140 and 240 μm, the *IRAS* maps at 24, 60 and 100 μm, and the *Planck* maps at 350, 550 and 850 μm (see Natale et al., in preparation). Good agreement was obtained between model and data at all wavelengths except at 1.2 μm, where the model underestimates the emission by 27 per cent. The origin of this discrepancy is discussed in Section 4.3 and will be addressed in future work. Thus, the optimization was done using all available bands except the 12 μm *IRAS* band. This band was not used as the 12 μm flux from the MW is dominated by emission from polycyclic aromatic hydrocarbons (PAH) in the diffuse ISM, and the abundance of PAH, though well calibrated at the solar circle, might be expected to vary with galactocentric radius, as is observed in external spiral galaxies. We used the IRIS maps generated from *IRAS* data by Miville-Deschênes & Lagache (2005), the *COBE*/(Diffuse Infrared Background Experiment) DIRBE maps from the CADE[2] and *Planck* maps obtained with the *Planck* High Frequency Instrument as described in Ade et al. (2014) and Planck Collaboration VIII (2016).

To avoid the optimization being overly influenced by nearby emission structures, both the model and observed maps were background-subtracted, using a background reference determined from strips offset from the galactic plane by $\pm 5^\circ$ in latitude. This also filters out any non-local structure on large scales due to a galactic halo. Since, in any case, it is difficult to distinguish between the contributions of distant halo emission and local emission from the galactic plane above the Sun, all predictions for the ISRF given in this paper are confined to the contributions from the galactic disc and bulge only.

The RT calculations were made using both a modified version of the 2D ray-tracing RT code of Kylafis & Bahcall (1987), as well as the 3D ray-tracing RT code DART-RAY (Natale et al. 2014, 2015). The 2D code uses the method of scattered intensities, introduced by Kylafis & Bahcall (1987) in an implementation by Popescu et al. (2000a), which (as in the original implementation of Kylafis) avoids obvious pitfalls recently highlighted by Lee et al. (2016), while preserving speed and accuracy, as demonstrated in Popescu & Tuffs (2013) and Natale et al. (2014). The 3D code provides an explicit calculation of all orders of scattered light. Results have been checked against each other using both codes. The linear resolution of the calculations was up to 25 pc, which is easily sufficient to model the resolved latitude profiles for structures at the galactic centre. In addition the data, which was highly resolved, showed no additional structure (e.g. a thinner layer in z) with sizes below the resolution of the code. For the optimization of the IR RFs, the relevant angular resolution is that of *IRAS* and *Planck* bands, which is 5′, corresponding to a linear resolution of approximately 12 pc at the galactic centre. The equivalent numbers for *COBE* (tracing direct stellar light from old stars in the NIR/MIR) is around 40′/90 pc.

The optical constants (from UV to submm) of the dust model used in the computations were those of Weingartner & Draine (2001) and Draine & Li (2007), whose grain model incorporated a mixture of silicates, graphites and PAH molecules. These optical constants are appropriate to model diffuse interstellar dust in the MW, as Draine & Li (2007) optimized the relative abundances and grain size distributions of the chemical constituents to fit the extinction law and IR/submm emissivity of translucent high latitude Cirrus dust clouds in the solar neighbourhood. The model for the dust emission incorporates a full calculation of the stochastic heating of small grains and PAH molecules. As described in PT11, our model accounts for possible variations in the IR/submm emissivities of grains in dense opaque molecular dust clouds by employing dust emission templates empirically calibrated on observed IR/submm emission spectra when accounting for the emission from such structures.

As in our model for external galaxies, the large-scale distribution of stars consists of an old stellar disc (‘the disc’), emitting in the optical/NIR, a UV- and optically/NIR-emitting young stellar disc (‘the thin disc’) and an optically/NIR-emitting bulge. In addition, to reproduce the observed latitude and longitude profiles in the inner disc in MW, we found that we needed to invoke a third component of stellar emissivity, consisting of both a very young stellar population, traced by the observed 24 μm emission in the inner disc, as well as an intermediate-age population, as seen in the NIR. We refer to this component of stellar emissivity as the ‘inner thin disc’. In our axisymmetric model, the bulge component is used to account for the combination of both the bulge and the inner bar of the MW, despite the geometry of the latter. All the stellar components are seen through a common distribution of diffuse dust. The diffuse dust is distributed into two discs associated with the old and young stellar populations, which we refer to as the ‘thick’ and ‘thin dust disc’ respectively, on account of the different thickness of these structures. Thus in our model of the MW the stellar volume emissivity and the dust density distributions for all the disc components i are described by the following generic formulae:

$$w_i(R,z|h_i,z_i)=\begin{cases} A_o\left[\dfrac{R}{R_{\rm in}}(1-\chi)+\chi\right]\dfrac{z_i(0)}{z_i(R)}\exp\left(-\dfrac{R_{\rm in}}{h_i}\right) \\ \times\mathrm{sech}^2\left(\dfrac{z}{z_i(R)}\right), \text{ if } R < R_{\rm in} \\ A_o\dfrac{z_i(0)}{z_i(R)}\exp\left(-\dfrac{R}{h_i}\right) \\ \times\mathrm{sech}^2\left(\dfrac{z}{z_i(R)}\right), \text{ if } R \geq R_{\rm in} \end{cases} \quad (1)$$

with:

$$z_i(R) = z_i(0) + (z_i(R_{\rm in}) - z_i(0))\left(\frac{R}{R_{\rm in}}\right)^{\gamma} \quad (2)$$

$$\gamma = \log\left(\frac{z_i(R_\odot) - z_i(0)}{z_i(R_{\rm in}) - z_i(0)}\right) / \log\left(\frac{R_\odot}{R_{\rm in}}\right) \quad (3)$$

[2] Centre d’Analyse de Données Etendues (CADE; Analysis Center for extended data) provides the *COBE* maps in the HEALPIX sky pixelization scheme at http://cade.irap.omp.eu/dokuwiki/doku.php?id=cobe

where h_i is the scalelength, $z_i(R)$ is the scaleheight dependent on the radial distance R, A_o is a constant determining the scaling of $w_\nu(R, z)$, χ is a parameter determining the ratio $w_\nu(0, z)/w_\nu(R_{\rm in}, z)$, $R_{\rm in}$ is a inner radius and $R_\odot$ is the galactocentric distance of the Sun, taken to be 8 kpc. One main difference between the generic formula for the MW given in equation (1) and that for external galaxies is that all stellar and dust components have, inside an inner radius $R_{\rm in}$, a decrease in their emissivities/opacities with decreasing radial distance, such that the emissivity/opacity at $R = 0$ kpc is a fraction χ of that at $R_{\rm in}$. Outside the inner radius, the stellar and dust emissivity/opacity of the discs are described by exponential functions in the radial direction. As in our modelling of external galaxies, we found a scalelength of the thick dust disc $h_{\rm d}$ that is larger than that of the old stellar disc, $h_{\rm s}$. This is also in accordance with the fact that external galaxies were found to have dust associated with extended H I discs, beyond the edge of the optically emitting discs (Popescu & Tuffs 2003; Bianchi & Xilouris 2011). For the vertical distribution we allow for a flare, by considering a general expression for $z_i(R)$ as given in equations (2) and (3). Thus, the generic function w of equation (1) is parametrized as:

$w_{\rm s}^{\rm disc} = w(R, z|h_{\rm s}^{\rm disc}, z_{\rm s}^{\rm disc})$ – for the stellar disc
$w_{\rm s}^{\rm tdisc} = w(R, z|h_{\rm s}^{\rm tdisc}, z_{\rm s}^{\rm tdisc})$ – for the thin stellar disc
$w_{\rm s}^{\rm in-tdisc} = w(R, z|h_{\rm s}^{\rm in-tdisc}, z_{\rm s}^{\rm in-tdisc})$ – for the inner thin stellar disc
$w_{\rm d}^{\rm disc} = w(R, z|h_{\rm d}^{\rm disc}, z_{\rm d}^{\rm disc})$ – for the thick dust disc
$w_{d}^{\rm tdisc} = w(R, z|h_{\rm d}^{\rm tdisc}, z_{\rm d}^{\rm tdisc})$ – for the thin dust disc

For the stellar bulge, we used a Sérsic distribution with Sérsic index 4, whose stellar volume emissivity $j_\nu(R, z)$ is defined as:

$$j_\nu(R, z) = j_\nu(0, 0) m^{\frac{-(2n-1)}{2n}} \exp\left(-C m^{1/n}\right) \quad (4)$$

with:

$$m = \frac{\sqrt{R^2 + z^2(a/b)^2}}{R_{\rm e}} \quad (5)$$

and $C = 7.67$ for $n = 4$.

Examples of stellar emissivity profiles in the J band and of dust opacity for the different stellar and dust components of our model for the MW are shown in Fig. 1. A summary of the values of the geometrical parameters of the model that are constrained from data is given in Table 1 and those that are adopted from PT11 are given in Table 2. The detailed explanation of how the values of these parameters were derived is given in Natale et al. (in preparation).

In addition to the large-scale distribution of diffuse dust and stars, the geometrical model also incorporates a clumpy component of dust physically associated with highly opaque, small filling factor birth clouds in the star-forming complexes. This clumpy component is taken to follow the same large-scale spatial distribution as the UV-emitting stellar populations in each of the two geometrically thin UV-emitting discs required to model the MW. Following PT11, a 'clumpiness factor' F is determined for each of these two UV-emitting discs. F is the total fraction of the non-ionizing light which is locally absorbed in the star-forming regions where the stars were born, giving rise to a local source of warm dust emission (i.e. typically prominent in the 25 and 60 μm bands). The thin disc was found to have a very high escape fraction of UV light from the star-forming regions, meaning the clumpy component of dust emission is negligible ($F = 0$). On the other hand, the inner thin disc was found to have a low escape fraction of UV light, with $F = 0.4$, so this geometrical component of dust emission is dominated (in luminosity terms) by the clumpy component of dust. Since the degree of local obscuration of UV light by the birth clouds can be quantitatively modelled in terms of the age of a UV-emitting stellar population (Tuffs et al. 2004), this provides new insight on the joint distribution over time and galactocentric radius of the recent SF activity in the MW. This is discussed further in Natale et al. (in preparation).

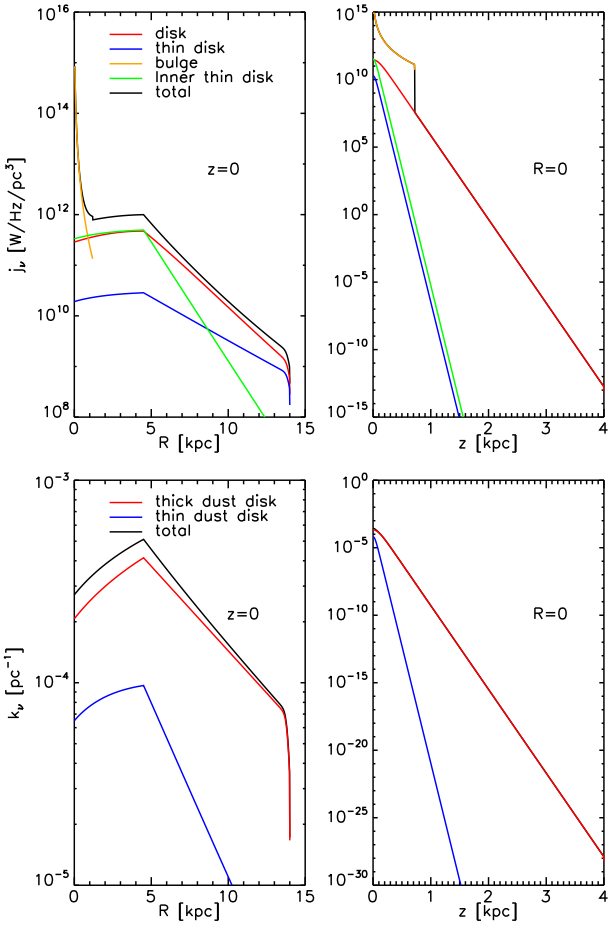

Figure 1. Top: radial (left) and vertical (right) profiles of stellar emissivity in the K band used in our model. The radial profile is for $z = 0$ kpc and the vertical profile is for $R = 0$ kpc. The different colours are for the stellar components of the model: disc (red), thin disc (blue), bulge (orange), inner thin disc (green). Bottom: same for dust opacity. The red line is for the thick dust disc and the blue line for the thin dust disc. The total emissivity/opacity is plotted in all panels with black.

Table 1. The geometrical parameters of the model that are constrained from data. All the length parameters are in units of kpc.

	Parameter	Uncertainty (per cent)
$R_{\rm in}$	4.5	5
χ	0.5	20
$h_{\rm s}^{\rm disc}(J, K, L, M)$	2.20, 2.20, 2.6, 2.6	25
$z_{\rm s}^{\rm disc}(0, R_{\rm in}, {\rm R}_\odot)$	0.14, 0.17, 0.30	25
$h_{\rm s}^{\rm tdisc}$	3.20	30
$h_{\rm s}^{\rm in-tdisc}$	1.00	+50 to 30
$z_{\rm s}^{\rm in-tdisc}(0, {\rm R}_\odot)$	0.05, 0.09	15
$h_{\rm d}^{\rm disc}$	5.2	15
$z_{\rm d}^{\rm disc}$	0.14	15
$R_{\rm eff}$	0.4	20
b/a	0.6	20

The values of the clumpiness factors F for the two UV-emitting discs are two of the global parameters of the MW in our model. The

Table 2. Constraints on geometry, following PT11.

$h_s^{disc}(B)/h_s^{tdisc}$	1
$h_s^{disc}(V, I)/h_s^{disc}(B)$	0.97, 0.80
$z_s^{tdisc}/z_s^{in-tdisc}$	1
h_d^{tdisc}/h_s^{tdisc}	1
z_d^{tdisc}/z_s^{tdisc}	1
$R_{trunc}/h_s^{disc}(B)$	4.4

others are the total face-on dust opacity in the B band at the inner radius $\tau_B^f(R_{in})$, the opacity ratio between the thick and thin dust discs $\tau_B^{f,disc}/\tau^{f,tdisc}$, the normalized luminosities of the thin discs, expressed in terms of a SFR for each disc (equations 16–18 from PT11), and the normalized luminosity (relative to some standard luminosity defined in PT11 to be 10 times the luminosity of the non-ionizing UV photons produced by a 1 $M_\odot$ yr^{-1} young stellar population) of the old stellar population 'old' (equation 12 from PT11). We note that it is the combination of F and SFR for each of the thin discs that controls the amplitude of the UV RFs in the diffuse ISM arising from each disc. In total our model has the 11 geometrical parameters listed in Table 1 (of which h_s^{disc} was independently determined in the J, K, L and M bands, and z_s^{disc} and $z_s^{in-tdisc}$ are optimized as a function of radial position describing the flare or taper) and eight amplitude parameters ($\tau_B^{f,disc}$, $\tau^{f,tdisc}$, SFR^{tdisc}, SFR$^{in-tdisc}$, F^{tdisc}, $F^{in-tdisc}$, old and B/D) that were constrained from data.

The best fit to the observed maps of the MW provided a solution with $\tau_B^f(R_{in}) = 1.48$, $\tau_B^{f,disc}/\tau^{f,tdisc} = 5.2$, a total SFR from the two thin discs of $1.25 M_\odot$yr^{-1} and old $= 0.35$. We adopt throughout this work the position of the Sun to be in the mid-plane at a galactocentric radius of 8.0 kpc.

The uncertainties in the main geometrical parameters of the model (those that are constrained from data) were derived by looking at the departure from the best-fitting model of only one parameter at a time, at the wavelength at which the parameter was optimized. For example, for the scalelength of the thick dust disc, h_d, we show in Fig. 2 how the fit to the averaged longitude and latitude profiles of surface brightness changes for a 15 per cent change in h_d (dotted lines). Because the large variation in amplitude was compensated for in the optimization by a subsequent variation in the amplitude parameter, $\tau^f(B)$, we also show the variation after the profiles were rescaled to fit the central flat part of the longitude profiles (shaded area). The shaded area is then taken to represent the uncertainty in the model fit. The corresponding variations from the best-fitting model in the RFs are shown in Fig. 3.

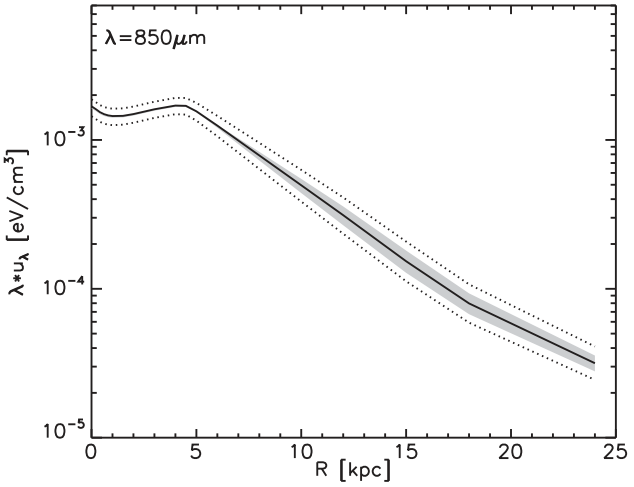

Figure 3. Variation in the radial profile of RFs (dotted lines) at 850 μm due to the 15 per cent variation in the h_d that can be tolerated by the fits to the longitude and latitude profiles at 850 μm. The shaded area represents the variation in the models after the same change in h_d, but this time accompanied by a change in the $\tau^f(B)$ parameter, such that the centre region of the 850 μm longitude profile is fitted. The shaded area thus represents the uncertainty of the RFs at this wavelength.

The uncertainties in the values of the geometric parameters estimated in this way are summarized in Table 1. Overall we estimate that the uncertainty in the main geometrical parameters is of the order 15 per cent–25 per cent, with the exception of $h_s^{in-tdisc}$, where the errors are large, +50 per cent and −30 per cent and for R_{in} where the errors are very small, of the order of 5 per cent. The errors in $h_s^{in-tdisc}$, optimized at 24 μm, are large because $h_s^{in-tdisc}$ is smaller than R_{in}, reflecting the fact that this parameter is the expression of a rather abrupt truncation of the luminosity in the inner disc. By contrast, the uncertainty in R_{in} is small since this determines the longitude at which the profiles flatten, which is a prominent feature of the observed profiles at all available wavelengths.

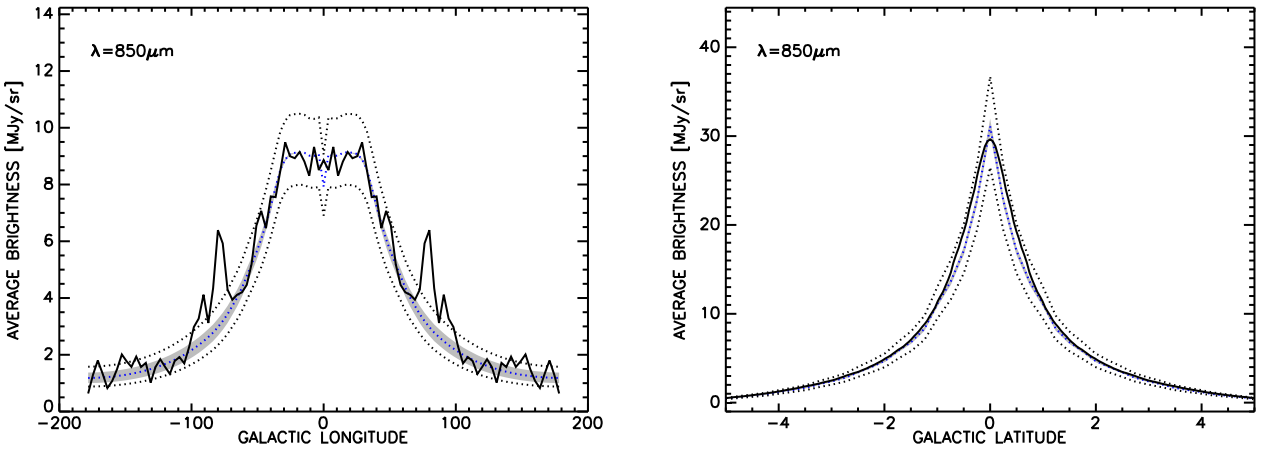

Figure 2. Variation in the averaged longitude and latitude model profiles (dotted lines) of surface brightness at 850 μm due to 15 per cent variation in the h_d. The corresponding observed profiles are plotted with a solid line. The shaded area represents the variation in the models after the same change in h_d but this time accompanied by a change in the $\tau^f(B)$ parameter, such that the centre region of the 850 μm longitude profile is fitted. This is equivalent to the conditional probability analysis conducted to find errors in h_d and $\tau^f(B)$.

3 COMPARISON BETWEEN MODELS AND DATA

As outlined in Section 2 and described in full detail in Natale et al. (in preparation), the model for the stellar and dust distribution of the MW was derived by fitting the detailed surface brightness distribution of stellar and dust emission from the NIR to the submm. To compare the model with data we show here in Section 3.1, a comparison between the model prediction for the integrated dust emission from the disc of the MW at the position of the Sun and the corresponding observed SED. In Section 3.2, we also show predictions for the local ISRF at optical/UV wavelengths, comparing these with the observational constraints. The fits of the model to the surface brightness distributions are shown in Natale et al. (in preparation).

3.1 The dust emission SED as seen from the position of the Sun

The IR volume emissivity distribution derived from the RT model of the Galaxy was used to derive the predicted brightness distribution maps of the entire sky, as observed from the position of the Sun. Corresponding maps of the observed dust emission were obtained at 12, 25, 60 and 100 μm from *IRAS*, at 140 and 240 μm from *COBE*, and at 350, 550 and the 850 μm from *Planck*. In order to avoid contamination with local structure or halo emission, not included in the model, both the model and observed maps were then integrated over a 10° wide strip in galactic latitude (i.e. the same area of sky used for the optimization) after subtracting a background from just outside the boundary of the strip in the same manner as done from the maps used in the optimization. The resulting comparison between the observed and predicted background-subtracted dust emission SED of the MW is shown in Fig. 4.

The error bars shown in the plot take into account uncertainties in the absolute photometric calibration of *IRAS*, *COBE* and *Planck* data, as well as uncertainties in the zodiacal light models, but do not take into account possible angular variations in the background light over the area of the 10 degree strip. A very good agreement between model and data can be seen, as is to be expected given that the model gives a good fit to the profiles in galactic latitude and longitude at all fitted wavelengths.

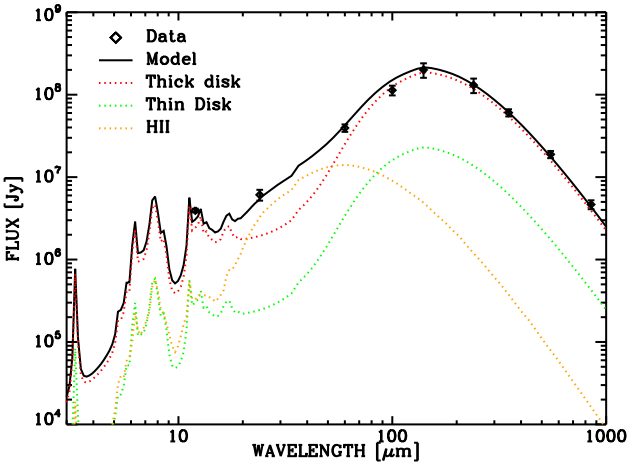

Figure 4. Comparison between the RT model predictions (solid line) and the IR data (symbols) for the background-subtracted integrated flux of the MW within a 10° strip in galactic latitude (±5°), as seen from the position of the Sun. The different colour dotted lines represent the different components of the dust emission model SED: the thick dust disc (red), the thin dust disc (green) and the clumpy component (orange). The data points at 12, 25, 60 and 100 μm are from *IRAS*, those at 140 and 240 μm are from *COBE*, and those at 350, 550 and the 850 μm are from *Planck*. The 850 μm map has been corrected for contamination from the CO $J = 3 \rightarrow 2$ line.

At 12 μm, our model slightly overpredicts the data, but, as noted in Section 2, this band is subject to uncertainties in the PAH abundance, and was not included in the optimization. At 100 μm, the model slightly overpredicts the observed flux, but careful examination of the detailed surface brightness distribution in the neighbouring bands at 140 and 60 μm, which are all consistent with the model and between themselves, suggests that there may be a small systematic error in the *IRAS* 100 μm flux calibration where the scan paths of the *IRAS* survey traversed the galactic plane (Natale et al., in preparation).

The agreement seen in the submm range justifies the distribution of dust opacity in the model. The agreement in the MIR, where the dust emission is predominantly powered by UV, means that the model prediction for the illumination of grains by UV light is also good, both in the diffuse ISM and locally in the SF regions. This is the most direct constraint of the global distribution of UV light in the MW, where direct measurement of UV light can only be performed for nearby stars. Finally, the correct prediction of the colour between the peak of the SED in the FIR and the MIR shows that both the SFR and the probability of escape of non-ionizing UV light from SF regions in the diffuse ISM, determined in the model by the *F* factor, are also correctly modelled. While Fig. 4 effectively shows the contribution of the galactic disc to the local ISRF at the position of the Sun, in Natale et al. (in preparation) we show that the predictions of our model for the surface brightness distribution in the 1.2–850 μm domain also agrees well with the observed distributions, confirming that the detailed spatial distribution of dust opacity and stellar emissivity, and thus the ISRF, is also correctly modelled throughout the volume of the MW.

3.2 Predictions for the local optical/UV interstellar radiation fields

The total intensity and the colour of the local UV/optical ISRF, as parametrized by Mathis, Metzer & Panagia (1983; MMP), is considered a benchmark quantity in the literature, with many measurements or model calculations given in units of the MMP ISRF. Since the MMP ISRF is a local measurement, it is very sensitive to nearby structure, in particular for shorter wavelengths where the range of photons is limited. It therefore does not provide a strong constraint of the model on global scales, as the IR maps of the MW do. It is nevertheless the only representation of the UV/optical ISRF based on some direct observations and for this reason we compare the observational data used to constrain the MMP ISRF with the predictions of our RT model in Fig. 5. This is a relatively challenging test of our determination of the UV/optical RFs, since no UV/optical data was used in our optimization analysis. Taking into account the proviso above, there is a good overall agreement between our model predictions and the MMP local ISRFs.

In passing we note that, in many studies relying on values for the ISRF, the approximation is made that the shape of the SED of the MMP local ISRF is the same as that of the SEDs of RFs at different galactocentric positions in our Galaxy or in external galaxies. This is despite the great range of variation in the colour of the RFs with position in a galaxy, as we have shown in Popescu & Tuffs (2013) for the PT11 model of external galaxies, and we now show below for the particular case of the MW.

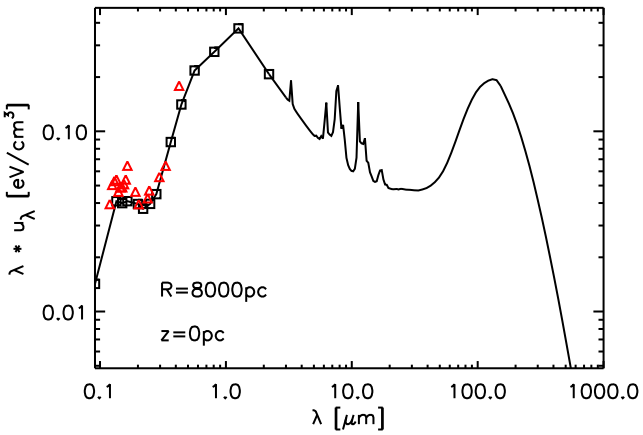

Figure 5. Comparison between our RT model prediction (solid line) of the local ISRF from the modelled structures of the MW, and the existing observational data. The red triangles are the data from Henry, Anderson & Fastie (1980) and from Witt & Johnson (1973). The squares are the sampling points of our model for the direct stellar light.

4 RESULTS

4.1 The radial and vertical profiles of the radiation fields

For the calculation of the RFs, we used an irregular grid which is better suited to sample the different morphological components of the model. In the radial direction, we give the results for 23 positions, with a variable spacing ranging from 50 pc in the inner disc to 6 kpc at a radial distance of 24 kpc. In the vertical direction, we calculate 22 positions, with a variable spacing ranging from 50 pc close to the disc plane and up to 2 kpc at a distance of 10 kpc above the disc.

The radial and vertical profiles of the RFs in direct stellar light in the MW reflect the detailed structure exhibited by the stellar emissivity of the different stellar components of our model, as well as the general characteristics of the fields originating from the three different vertical structure components emitting stellar photons in our model, the disc, the thin disc and the bulge, as described in Popescu & Tuffs (2013; PT13). This can be seen in the examples given in Fig. 6, where we plotted the radial profile in the plane of the disc and at 1 kpc above the disc, as well as the vertical profile in the centre of the disc and at a radial distance of 8 kpc. The profiles were plotted for an NIR, an optical and a UV wavelength.

Inspection of the radial profiles in the plane of the disc (see upper left panel of Fig. 6) in the K band shows that the inner 0.5–5 kpc is rather flat, due to the decrease in the stellar emissivity and dust opacity with decreasing radial distance within the inner radius $R_{\rm in}$. If the emissivity and opacity profiles were to increase exponentially throughout the centre, then the RFs would be expected to decrease monotonically at this wavelength, following the optically thin solutions of the disc described in PT13. In the B band, the profile within the 0.5–5 kpc not only flattens, but even decreases with decreasing radial distance, due to the additional effect of increasing the optical depth at this wavelength. As described in section 5.3 of PT13, for a pure exponential disc, the RFs are expected to flatten in the inner region. The same trend is visible in the UV. In the inner 0.5 kpc, the RF are dominated by the bulge component.

Outside $R_{\rm in}$, the solutions for the RF follow the general trends predicted for exponential discs in PT13. In the UV, the solutions are dominated by the thin disc, with the characteristic shallow monotonic decrease. The break in the UV profile at around 14 kpc is due to the assumed stellar truncation. The very prominent break of the UV profile is due to the optically thick character of the solution for the thin disc. In the B band, where the disc is less opaque at these radii, the truncation becomes less pronounced in the profiles of RFs, with the profile tending to a R^{-2} dependence beyond 18 kpc. In the K band, the solution is optically thin. Therefore, the truncation is not visible in the profile, but rather the profile tends smoothly towards the R^{-2} dependence.

At 1 kpc above the plane of the disc (see upper right panel of Fig. 6), the radial profiles of the RFs are only dominated by the disc and inner thin disc in the K and B bands, since at that distance (more than one $R_{\rm eff}$ of the bulge), the cuspiness in the stellar emissivity of the bulge disappears. As expected from PT13, the UV profile becomes rather flat up to large radii. This is due to the fact that the thick dust disc, rather than the thin dust disc, controls the emission escaping from the thin disc (see detailed explanation in PT13).

The vertical profiles in the centre of the MW (see lower left panel of Fig. 6) show again the dominance of the disc and inner thin disc in the K and B bands, except for the inner ∼0.5 kpc, where the cuspiness is due to the bulge. The UV profile shows the general characteristics of the thin disc, namely a monotonic decrease above the disc, followed by a flat plateau at relatively large vertical distances, which eventually steepens to an R^{-2} dependence. The flattening of the profile was explained in PT13 as a consequence of the optically thick character of the solution and of the two dust disc structure. Thus, a vantage point at larger vertical distances above the disc will essentially see a constant surface brightness until large radii.

At larger radii (see lower right panel of Fig. 6), the vertical profiles are rather flat in all cases, because the typical distance to the emitting regions, irrespective of whether they are optically thin or thick, does not change much. The bumps at around 3 and 6 kpc are an artefact of the RT calculations, and could be reduced by increasing the computation time.

In Fig. 7, we show examples of uncertainties in the RFs arising from the combined uncertainties in the geometrical parameters listed in Table 1. In the UV, the uncertainties are dominated by the uncertainty in the parameter $h_{\rm s}^{\rm tdisc}$, which is optimized at 240 μm, and to a lesser extent by the uncertainty in the parameter $h_{\rm d}^{\rm disc}$, which is optimized at 850 μm. At radii smaller than $R_{\rm in}$, the uncertainties in the RFs are very small, because the RFs are primarily determined by the χ parameter and the SFR, which are both quite precisely derived. In the B band, the errors are smaller than in the UV, but this is due to the fact that no source of error was incorporated for the parameter $h_{\rm s}^{\rm disc}(B)$, since this was fixed rather than constrained from data.

In the FIR and submm, the galaxy is optically thin, and therefore the RFs follow similar trends to those seen in the stellar RFs in the K band. This can be seen in both the radial and vertical profiles of dust emission (see examples from Fig. 8). Thus, the radial profiles in the plane of the disc outside $R_{\rm in}$ (see top right panel of Fig. 8) show that at all IR wavelengths the profiles monotonically decrease with increasing wavelength. The remaining profiles in Fig. 8 are again similar to the corresponding K-band profiles from Fig. 6. The vertical profiles from the bottom right panel of Fig. 8 show a steep increase as z tends to zero, not seen in the stellar profiles at the K-band wavelength. This is because in an optically thin case, the smaller the scaleheight of the emitters, the higher the emission closer to the disc plane is. Since most of the dust emission originates from discs that are thinner as compared with the thicker stellar disc in the K band, it is clear that the RFs of dust emission will have a higher enhancement close to the plane of the disc.

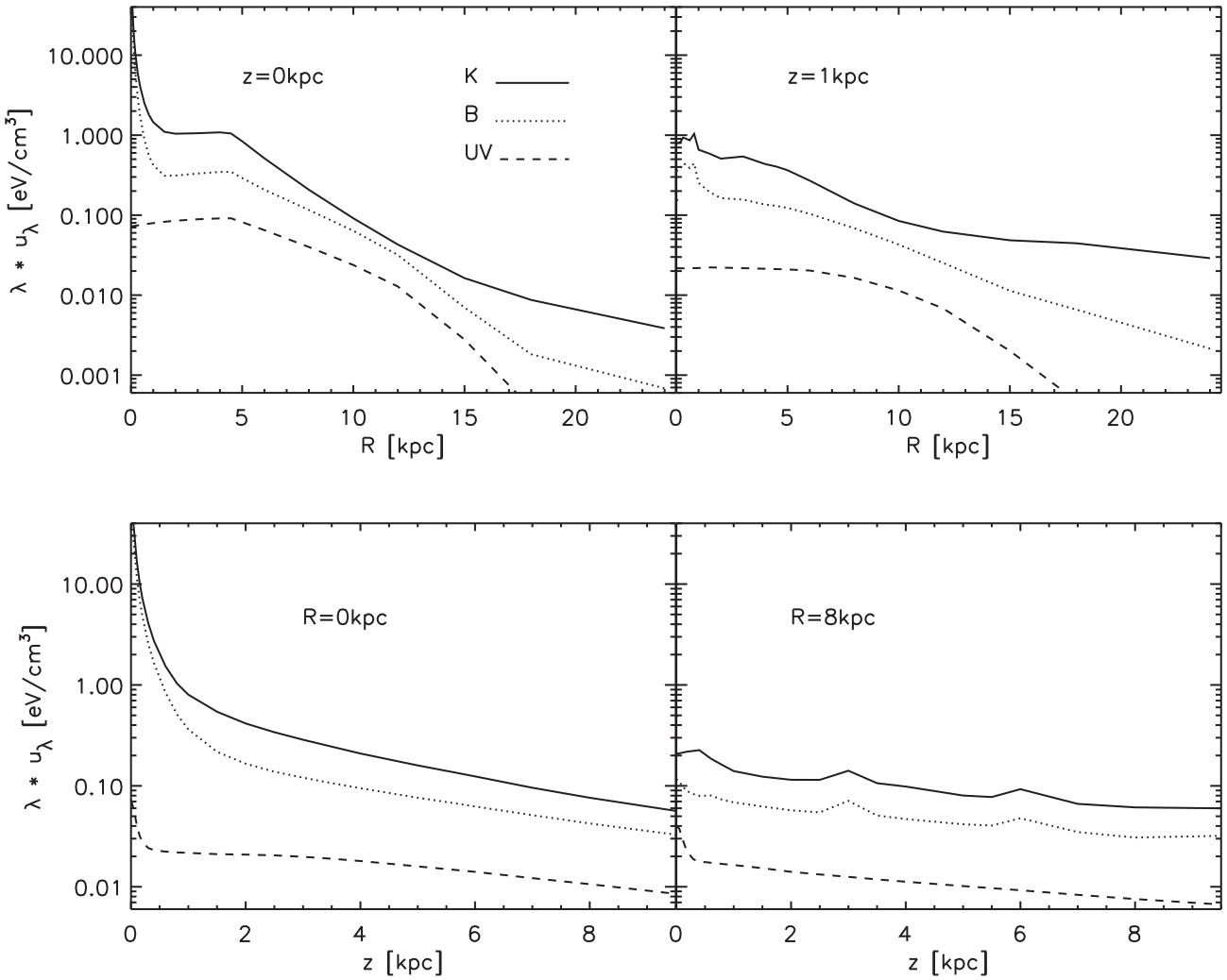

Figure 6. Top: radial profiles of RFs in direct stellar light at $z = 0$ kpc (left) and at $z = 1$ kpc (right). Bottom: vertical profiles of RFs at $R = 0$ kpc (left) and $R = 8$ kpc. The different lines correspond to the profiles at 2.2 μm (solid line), 4430 Å (dotted line) and 1500 Å (dashed line).

The uncertainties in the dust emission RFs are small in relation to those in direct stellar light, similar to those plotted in Fig. 3. This is because there is a very direct empirical link between the RFs and the *IRAS* and *Planck* data, from which the bulk of the geometrical parameters were optimized. This is also coupled to the fact that the galaxy is transparent at the FIR–submm wavelengths.

4.2 The SEDs of the radiation fields

One important characteristic of the RFs is their spectral distribution. For applications to high-energy astrophysics, it is particularly important to accurately derive the relative proportions of FIR, optical and UV photons, as this would determine the spectral distribution of gamma-ray photons originating from IC scattering of the RFs.

To this end, we show in Fig. 9 examples of SEDs of RFs at different positions in the MW. It is interesting to note that the SEDs of the RFs in the centre regions (see top panels) have a strong peak in the NIR, which is due to the prominence of the stellar bulge and of the inner disc, and a secondary peak in the FIR. The ratio between the NIR and FIR peaks remains approximately constant when going from (1,0) kpc to (1,1) kpc above the disc, since both the NIR and FIR RFs decrease by approximately the same factor, as expected due to the optically thin character of the solutions in both spectral ranges (see right top panel of both Figs 6 and 8).

At larger radial distance in the plane of the disc (see bottom panels of Fig. 9), the NIR and FIR peaks of the SED become comparable. This is due to the fact that the NIR range is no longer affected by the stellar bulge and the inner disc. For the same reason, the NIR-to-UV ratio is also decreased substantially in comparison with the inner parts of the disc.

The FIR SED of the RFs peaks at shorter wavelengths in the central parts of the disc, due to the strong heating of the dust in the central regions, including the heating from the bulge and the inner disc.

4.3 Applicability and limitations of the predicted radiation fields

The main caveat of our model of the MW is the assumption that the properties of the dust grains follow the model of Weingartner & Draine (2001). In this model, the absorptivities and emissivities of the different grains, although empirically anchored through laboratory measurements in the UV/optical/NIR/FIR range, are quite uncertain in the submm. If the submm grain efficiencies

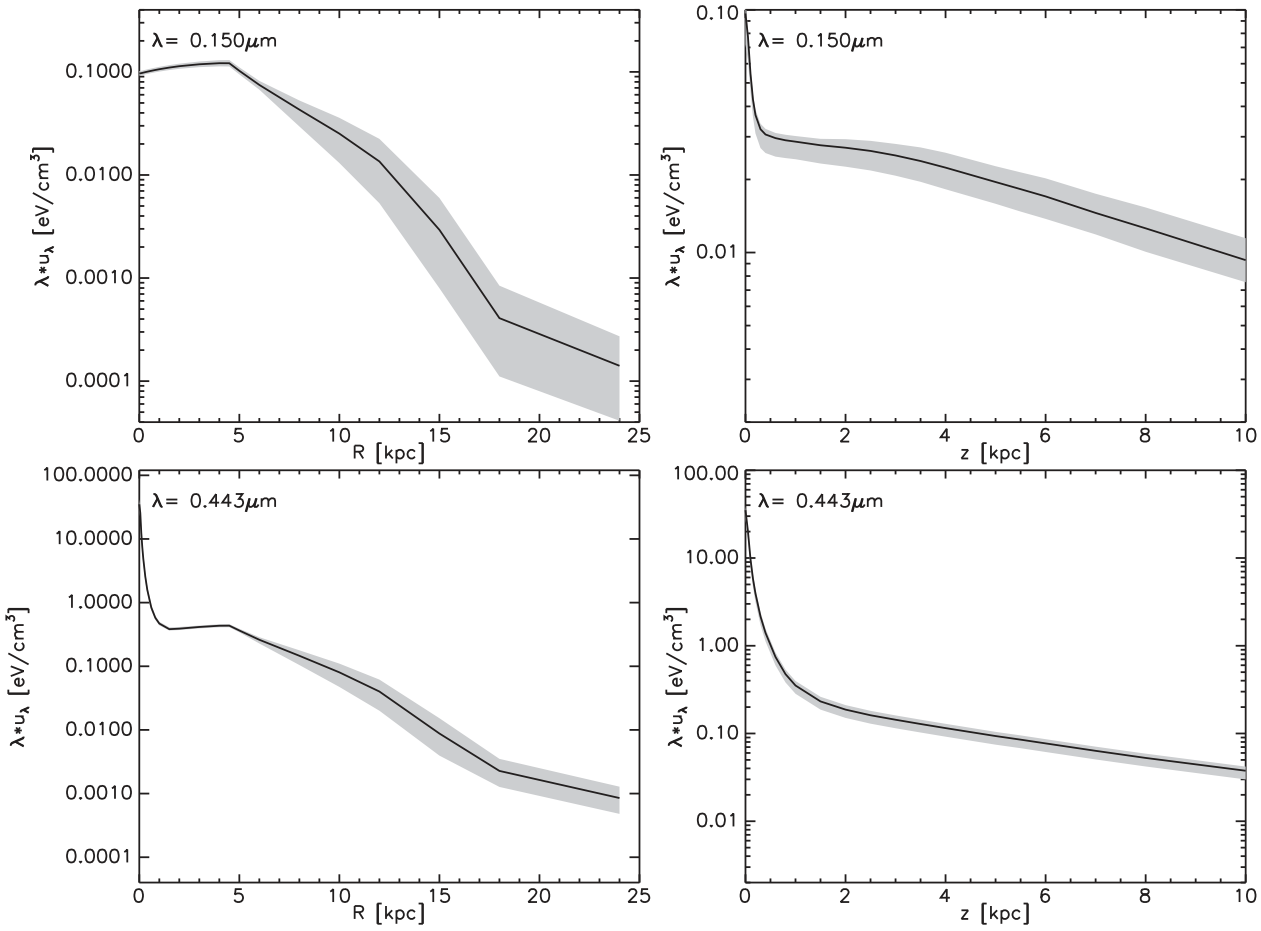

Figure 7. Examples of the uncertainties (shaded area) in the RFs in direct stellar light arising from the combined uncertainties in the geometrical parameters listed in Table 1. The solid line shows the RFs for UV 1500 Å and *B* band, as plotted in the left-hand column of Fig. 6.

were higher than the predictions of the WD01 model, as recently suggested by the Planck Collaboration XXIX (2014), this would be equivalent to an overestimation of the UV–optical depth of the galaxy for a model that assumes WD01 dust. However, in the case of our analysis of the MW, we largely constrain the amplitude, intrinsic colour and geometric distribution of the UV–optical RF through the predictions of amplitude, colour and geometric distribution of the MIR/FIR dust emission. Thus, the solution for the UV–optical energy densities themselves will be largely invariant to the choice of dust model, since, irrespective of whether or not the use of the WD01 model has led to an overestimation of the UV–optical depth, one would have exactly the same detailed energy balance between UV and optical energy absorbed and IR energy emitted, and exactly the same spatial structure in this detailed balance. This statement holds exactly for the RFs in the UV and optical (*B*, *V*, *I*) range, since the emission from the MW as a whole at these wavelengths is anyway inaccessible to direct observation, so has to be found exclusively through fitting the dust emission data under the assumption that the geometrical scale ratios follow the constraints from PT11 (see Natale et al., in preparation). This invariance of the ISRF to the choice of the dust model will only break down in the NIR, since there we do determine the amplitude and spectrum of the stellar emission by fitting the NIR imaging of the directly observed stellar light. However, we also find that the UV–optical RFs, as derived from the FIR data, are robust against changes in the parameters of the NIR emissivity. This is largely because the NIR emission is not dominant in the dust heating. We can therefore conclude that the solutions in the UV/optical (*B*, *V*, *I*) and MIR/FIR/submm for the RFs presented in this paper are relatively robust against the choice of dust model, but that the NIR solutions would be altered should the dust model be different. A dust model with higher submm efficiencies may potentially account for the underestimation of the *J*-band luminosity in the present solution, but this would need to be quantitatively investigated in future work. Here, we present the solution for the RFs of a MW having a WD01 dust type.

An obvious limitation of our model is our imposition of axial symmetry, which is none the less crucial in breaking the luminosity–distance degeneracy and in providing a robust way to derive geometrical distributions independent of prior knowledge coming from stellar counts or gas measurements. Clearly, we cannot therefore predict variations due to the boxy-peanut shape of the bulge/bar structure in the inner disc. This may also account for the underprediction of the *J*-band luminosity, although again this needs to be quantitatively addressed in future work. Also, we cannot predict the variations in the diffuse ISRF expected between the arm and inter-arm regions. Tendentially, we will underpredict the ISRF in the arms, and overpredict it in the inter-arm regions. Nevertheless, because the volume of the inter-arm regions dominates the volume of the galaxy, our solutions should only very slightly over predict the true diffuse ISRF over the bulk of the volume of the galaxy.

The boost in the ISRF in the arms will be strongest in optically thin bands, such as in the NIR/MIR/FIR/submm. In optically thick

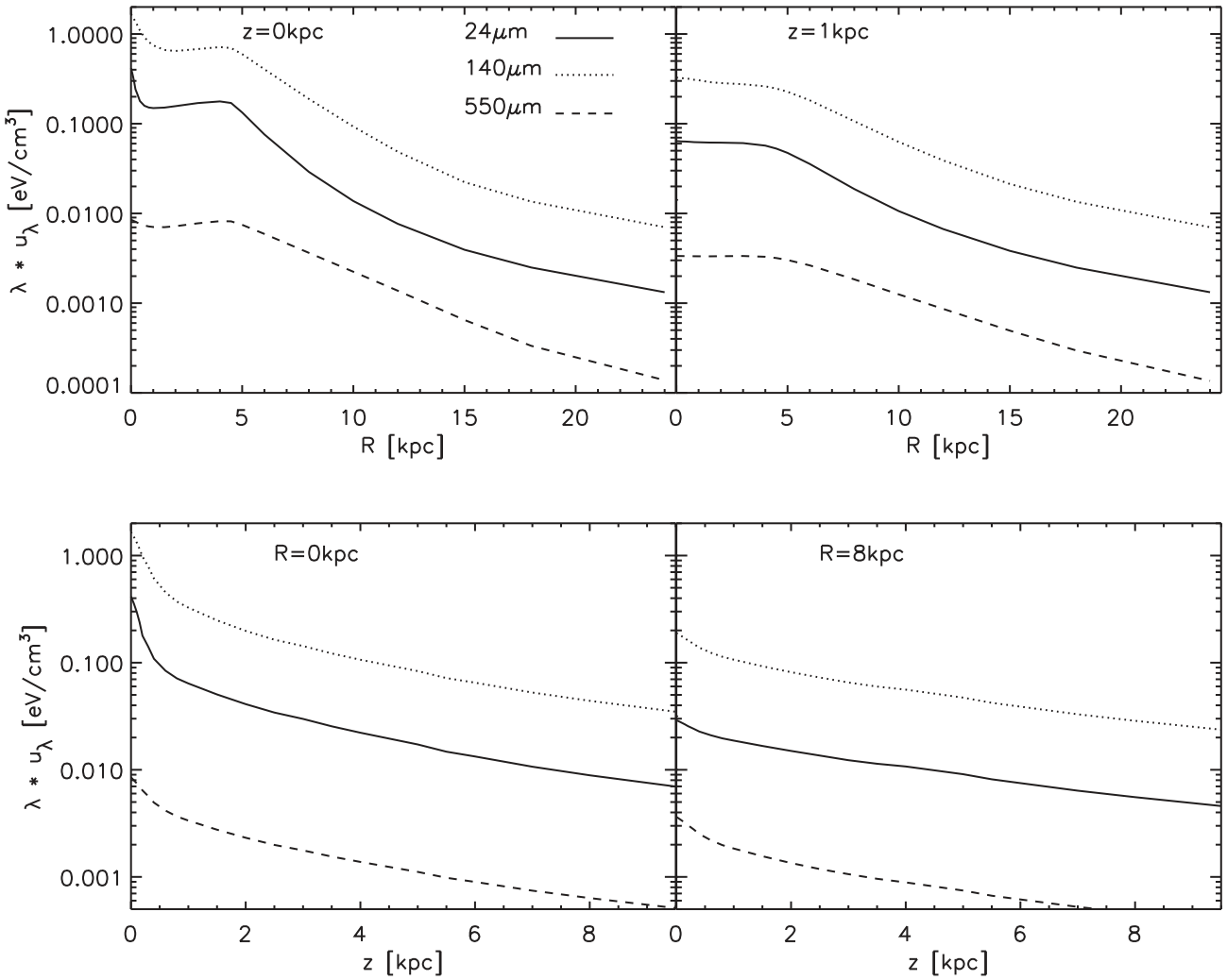

Figure 8. Top: radial profiles of RFs in dust emission at $z = 0$ kpc (left) and at $z = 1$ kpc (right). Bottom: vertical profiles of RFs at $R = 0$ kpc (left) and $R = 8$ kpc. The different lines correspond to the profiles at 24 μm (solid line), 100 μm (dotted line) and 350 μm (dashed line).

structures, such as spiral arms in the optical, the *in situ* ISRF will scale as the ratio of emissivity to opacity, which, in the case of a purely compressive structure like a spiral density wave, should, to first order, not affect the *in situ* diffuse ISRF. It is also partly because of this that the emergent SEDs of galaxies modelled with spiral arms is only marginally different to galaxies with the same global parameters, but modelled as completely smooth discs (as demonstrated in PT11).

In general, therefore, one can regard the model predictions for the ISRF as very close to the true ISRF over most of the volume, whereby the true ISRF will only strongly exceed the model predictions in spiral arms and the bar in the IR, and near powerful discrete sources. In practice, this means that one can use the model to place lower limits on the IC emission component of the gamma-ray emission when modelling individual high-energy emission sources. When modelling the global IC component of the gamma-ray emission of the MW from scattering off the ISRF, the model should, analogous to its prediction of the observed longitude and latitude profiles in the IR, give a systematically correct prediction of the IC emission profiles from smoothly distributed CR electrons in the ISM, subject only to moderate undulations due to the spiral and bar structure. We should point out that whereas the model can be used to predict the IC emission from the general population of CR interacting with the ISRF, it can only be used to place lower limits to the component of IC of any localized sources of CR geometrically associated with SF regions.

Another fundamental assumption of the model is that the dust not associated with SF regions is diffusely distributed. We know that this is actually not the case, since when looking at high-resolution *Herschel* images of the plane of the MW one sees that this dust is actually distributed in an intricate pattern of filamentary structure. However, individually these filaments are at a good approximation optically thin to the ISRF, so for the purpose of calculation of transport of photons, one does not need to explicitly treat these structures as clumps. The one caveat to this is that the detailed structure we see at high latitude on the *Herschel* images are very local to the Sun, so do not give direct observational constraints on the presence and optical depth of passive small-scale structures in the centre of the MW. If these structures were optically thick, our model would overestimate the attenuation of starlight from the inner disc.

We also draw attention again here to the fact that our model for the ISRF does not include any component of ISRF from a possible large-scale emission component from a galactic halo, where

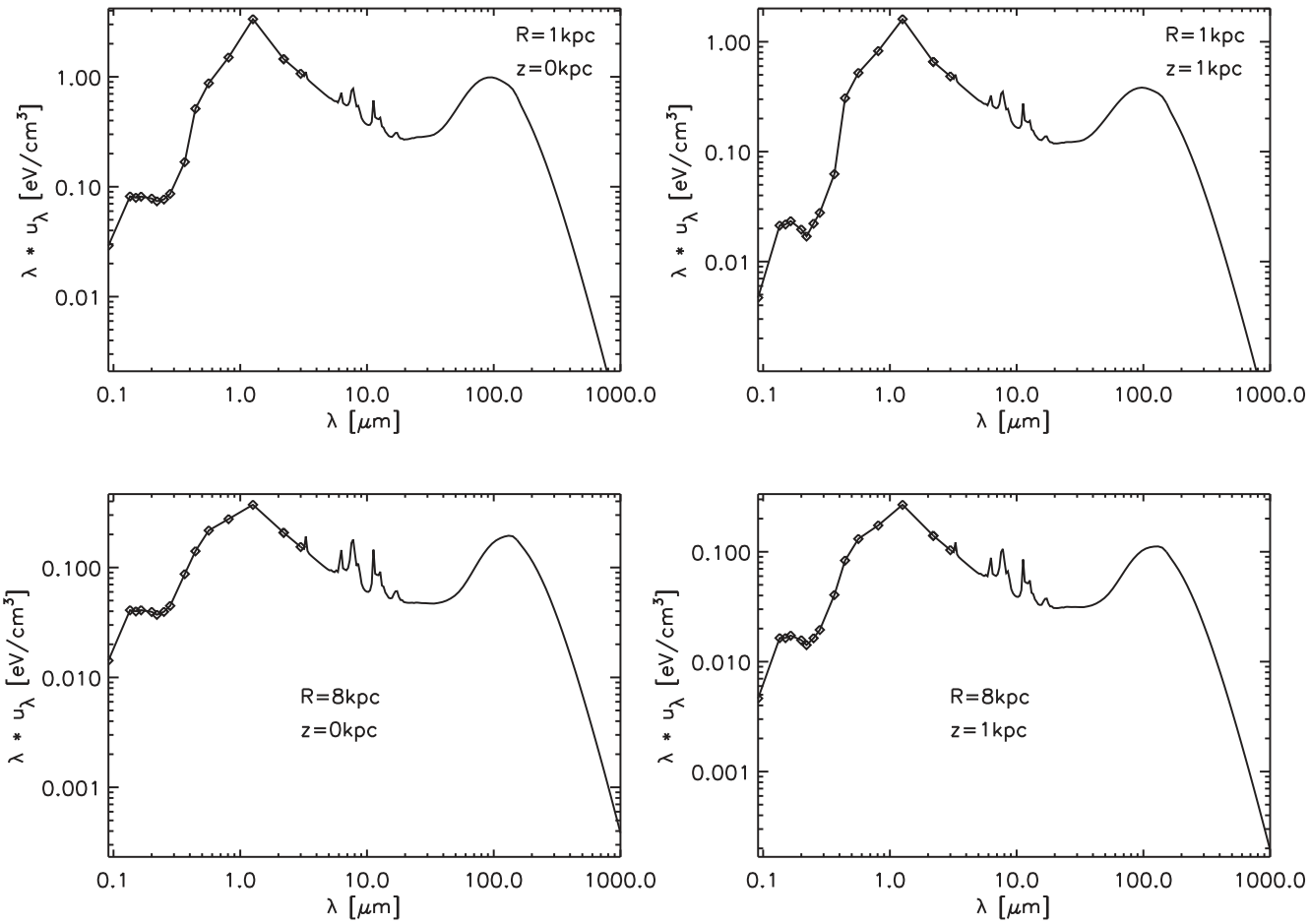

Figure 9. SEDs of RFs at various galactocentric positions. The symbols are for the UV/optical wavelengths at which the RT calculations were performed. For the dust emission, the calculations were performed at 500 wavelengths, logarithmically spaced.

diffuse dust could be collisionally heated with ambient hot plasma (Popescu et al. 2000b). We refrained from doing this in this work due to the difficulty in distinguishing between observed smooth emission components extending over the sky due to local emission above the Sun, and a truly large-scale (and thus much more luminous) halo emission component. The implications of this for the predicted ISRF are in any case negligible in the FIR, because at these wavelengths only a very small fraction of the observed total integrated flux over the whole sky does not arise from the modelled disc structure. However, at 25 μm and shorter wavelengths, a significant (though still minority) fraction of the observed all-sky flux cannot be accounted for by the model for the disc and bulge structures of the MW, indicating another origin. Nevertheless, even if originating from a large halo, this addition MIR luminosity source would significantly boost the ISRF in the plane of the galaxy only at the solar circle and beyond. The main observational consequence to gamma-ray astronomy of the existence of an MIR-emitting galactic halo, should this be shown to exist, would instead be some increase in the predictions for the pair-production opacity of VHE gamma rays, beyond the predictions we give in Fig. 14 of this paper. We will return to the nature of the MIR background emission in a future work.

Table S1 (included in the electronic submission only) gives the values for the total local ISRF at the Solar position, $u_{\lambda,\mathrm{total}}$, in each of the bands of *COBE*/DIRBE, *IRAS* and *Planck*, obtained from the total all-sky flux S_{allsky} observed on the maps, calculated through the relation:

$$u_{\lambda,\mathrm{total}} = \frac{1}{\lambda^2} \times S_{\mathrm{allsky}} \tag{6}$$

Table S1 also gives the corresponding values for u_λ for the model, $u_{\lambda,\,\mathrm{model}}$. The difference $u_{\lambda,\,\mathrm{background}} = u_{\lambda,\,\mathrm{total}} - u_{\lambda,\,\mathrm{model}}$ then gives the contribution to the local ISRF from the background emission which was excluded in our analysis of background-subtracted strip maps of width $\pm 5^\circ$ in latitude. We will return to the question of whether this background component is from the galactic halo, rather than being local, in a future work.

5 COMPARISON WITH THE RADIATION FIELDS PREDICTED BY THE GALPROP MODEL

To date, the GALPROP model has been the only one providing calculations for the RFs in the MW (Strong et al. 2000; Moskalenko et al. 2002; Porter et al. 2006; Moskalenko et al. 2006; Porter et al. 2008). This model has been extensively used by the high-energy community for the interpretation of the gamma-ray emission. For this reason, we compare the solutions for the ISRF of our RT model with the RFs from GALPROP.[3] Here we show a few comparative

[3] The RFs from GALPROP were taken from http://galprop.stanford.edu/, using data files from GALPROP v.54. The files with the RFs are taken from the files /ISRF/Standard/Standard_x_0_z_flux.dat.

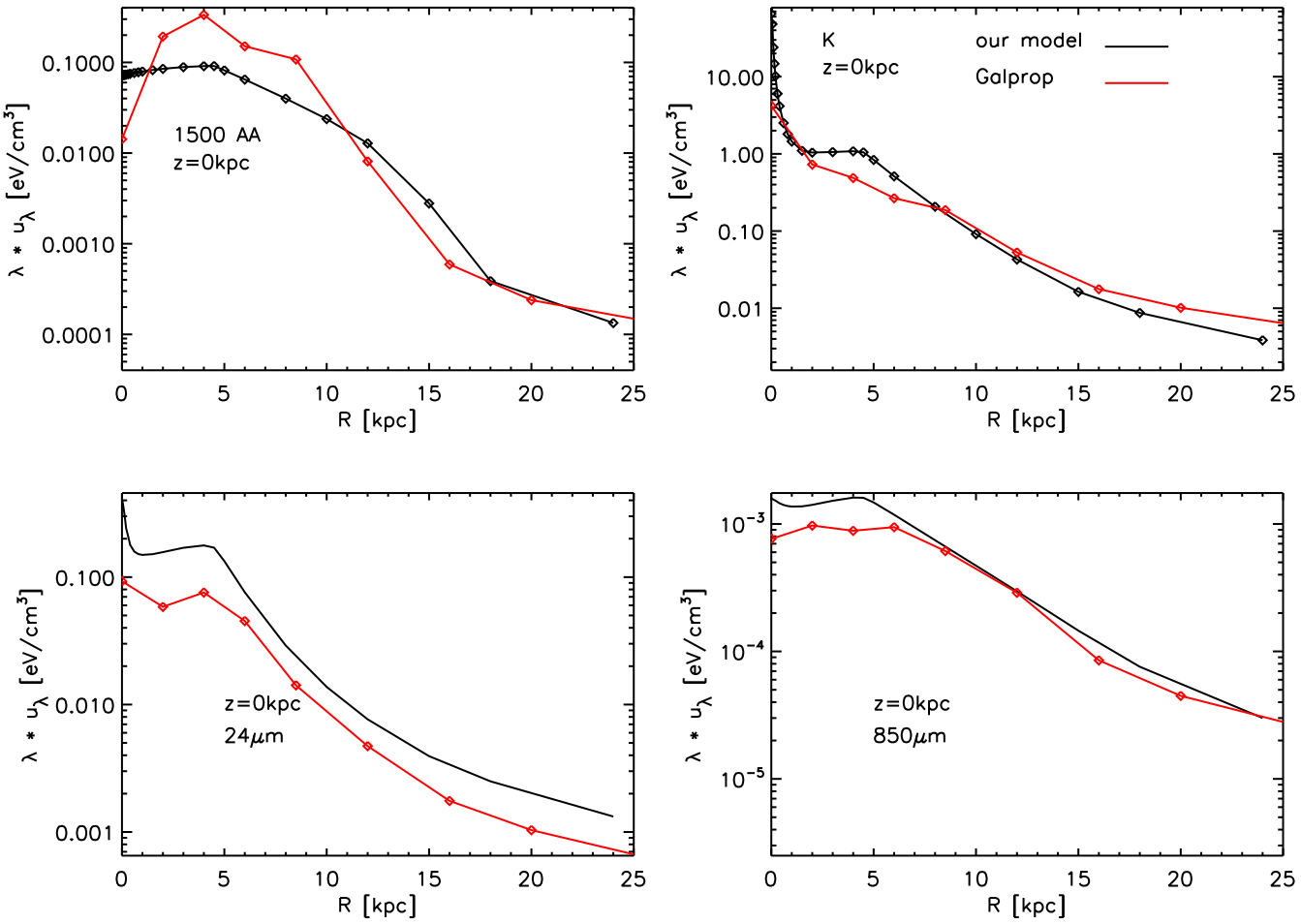

Figure 10. Comparison between the mid-plane radial profiles of the RFs predicted by our RT model (black line) and the GALPROP model (red line) for selected wavelengths. The symbols show the sampling points in both models.

plots for four selected wavelengths, at 1500 and 22000 Å in the UV and NIR, and at 24 and 850 μm in the MIR and submm. In Fig. 10, we plot mid-plane radial profiles and in Fig. 11 we plot central vertical profiles. We find that overall there are systematic differences between the GALPROP RFs and those predicted by our model, in particular in the UV and in the MIR. Since GALPROP uses the same model for the size distribution and optical properties of the grains (Weingartner & Draine 2001; Draine & Li 2007) as our model, the differences must be found in the different geometry considered for the stellar and dust distributions. Indeed, inspecting the recent comparison between the GALPROP predictions and the *IRAS*/*COBE*/*Planck* maps shown in Porter (2016) it appears that the geometry used in the GALPROP model is not consistent with the observational data. This reflects the different concepts involved in the two models. Thus, GALPROP assumes the stellar and dust distributions to be known and an input to the model, while our model derives the stellar and dust distributions as an output of the model. In doing this GALPROP imports distributions derived from stellar counts and gas measurements, while we optimize the distributions on the *IRAS*/*COBE*/*Planck* maps.

There may be also some technical differences in the modelling itself. Thus, a major reason for the difference in the predictions for the MIR emission could be the treatment of dust locally heated by radiation from young stars in the parent molecular clouds of star-forming regions. This process, which takes place on parsec scales, is the main contributor to the energy emitted by a galaxy in the 24–70 μm (see Popescu et al. 2000a). As outlined in Section 2, our RT model incorporates this process by calculating the absorption of radiation in an ensemble of opaque, but fragmented star-forming clouds. The GALPROP model does not take into account this process, but only assumes a diffuse large-scale distribution of stellar emissivity and dust (Porter et al. 2008). Neglecting the mechanism of locally heated dust emission is thus one potential reason why the bulk of MIR emission from the MW would be missed by GALPROP.

Another possible reason for the discrepancy in the MIR could come from differences in the way the diffuse component of the MIR emission is calculated by the two models. This emission arises from stochastically heated small dust grains and PAH molecules. The transition between emission arising from grains heated to an equilibrium dust temperature and those heated impulsively depends both on the size of the emitting particle but also on the strength and colour of the ISRF. This transition needs to be therefore self-consistently calculated for each grain at each position in the galaxy. Our RT model incorporates a self-consistent calculation of this transition (see Popescu et al. 2011). However, the GALPROP model considers a fixed size where this transition occurs (Porter et al. 2008), independent on the strength and colour of the RFs. This could lead to a systematic underprediction of the diffuse MIR emission in the outer regions of the MW, and an overprediction of the MIR

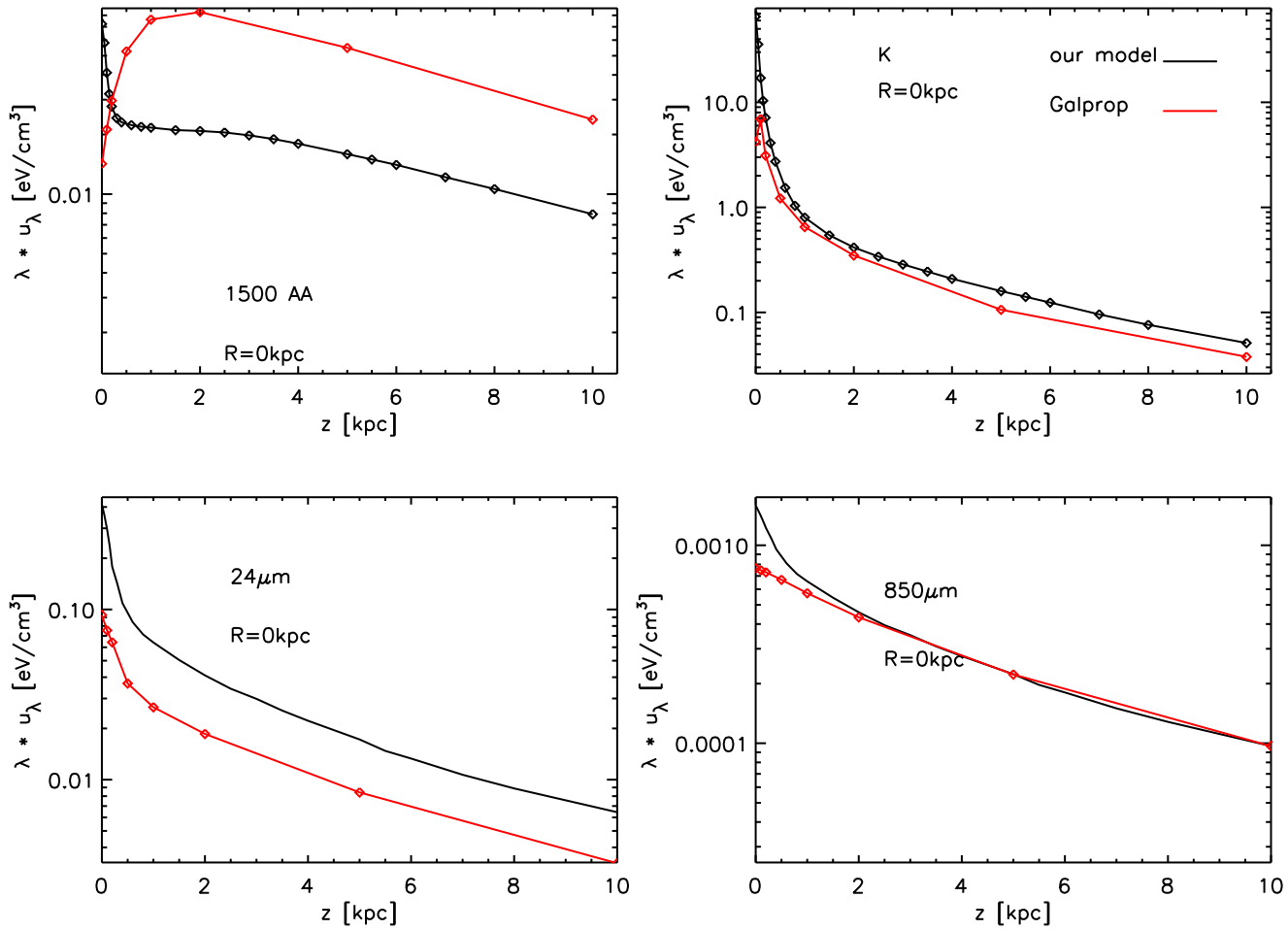

Figure 11. Comparison between the central vertical profiles of the RFs predicted by our RT model (black line) and the GALPROP model (red line) for selected wavelengths. The symbols show the sampling points in both models.

emission in the inner regions. This could add to the discrepancies seen in the comparative plots, although this cannot be a major factor.

Recently, Porter (2016) has advocated that the reason the 2D GALPROP model fails to reproduce the observed maps in the NIR, FIR and submm is due to the axisymmetric nature of the model, and a 3D model is proposed instead. While a detailed 3D model is indeed desirable to account for the detailed inner bulge-bar regions of the MW, our analysis shows that an axisymmetric model is well able to reproduce the overall observed multiwavelength large-scale surface brightness distributions.

6 THE EFFECT OF THE RADIATION FIELDS ON THE INVERSE COMPTON EMISSION AND THE GAMMA-RAY OPACITY

In this section, we explore how the spatial and spectral distribution of the ISRF in the MW affects the spatial and spectral distributions of the gamma rays produced via IC scattering, as well as the attenuation of the gamma rays due to interactions of the gamma-ray photons with photons of the ISRF. We make no attempt to model the spatial and spectral distributions of the CR electrons, but rather take a standard reference distribution in electron energy to illustrate the imprint of the ISRF on the processes considered and we make the assumption that the electron spectrum is the same everywhere in the galaxy. In reality, the electron spectrum can vary with position, especially at TeV energies. Moreover, electrons with energies above 10 TeV cannot propagate more than 100 pc, therefore their spectrum should vary with position. However, because in this paper we only want to illustrate the impact of the ISRF on the predictions for the gamma-ray emission, we consider the simplest assumption of a homogeneous distribution of electrons. Specifically, we assume the electron spectra at each position in the MW to be given by a power law with an index of -3 and a high-energy exponential cut-off E_b ($5.4 \times 10^{-12}\,(E/1\mathrm{GeV})^{-3}\exp(-E/E_b)\,\mathrm{cm}^{-2}\,\mathrm{s}^{-1}\,\mathrm{GeV}^{-1}$) with a normalization given by the electron flux measured by PAMELA (Adriani et al. 2011) at 10 GeV.

6.1 Inverse Compton scattering

To calculate IC scattering, we adopt the formalism described in Khangulyan, Aharonian & Kelner (2014). In the current calculation, we neglect the anisotropy in the target photon field, although we note that anisotropy may cause significant enhancement of the high-latitude diffuse emission (Moskalenko & Strong 2000). This issue will be addressed in our future work.

In Fig. 12, we show the predicted gamma-ray IC SEDs for different positions in the MW, and for different cut-off energies E_b of the electron spectra. In each case, we also show the predicted gamma-ray IC SED resulting just from the CMB photon field.

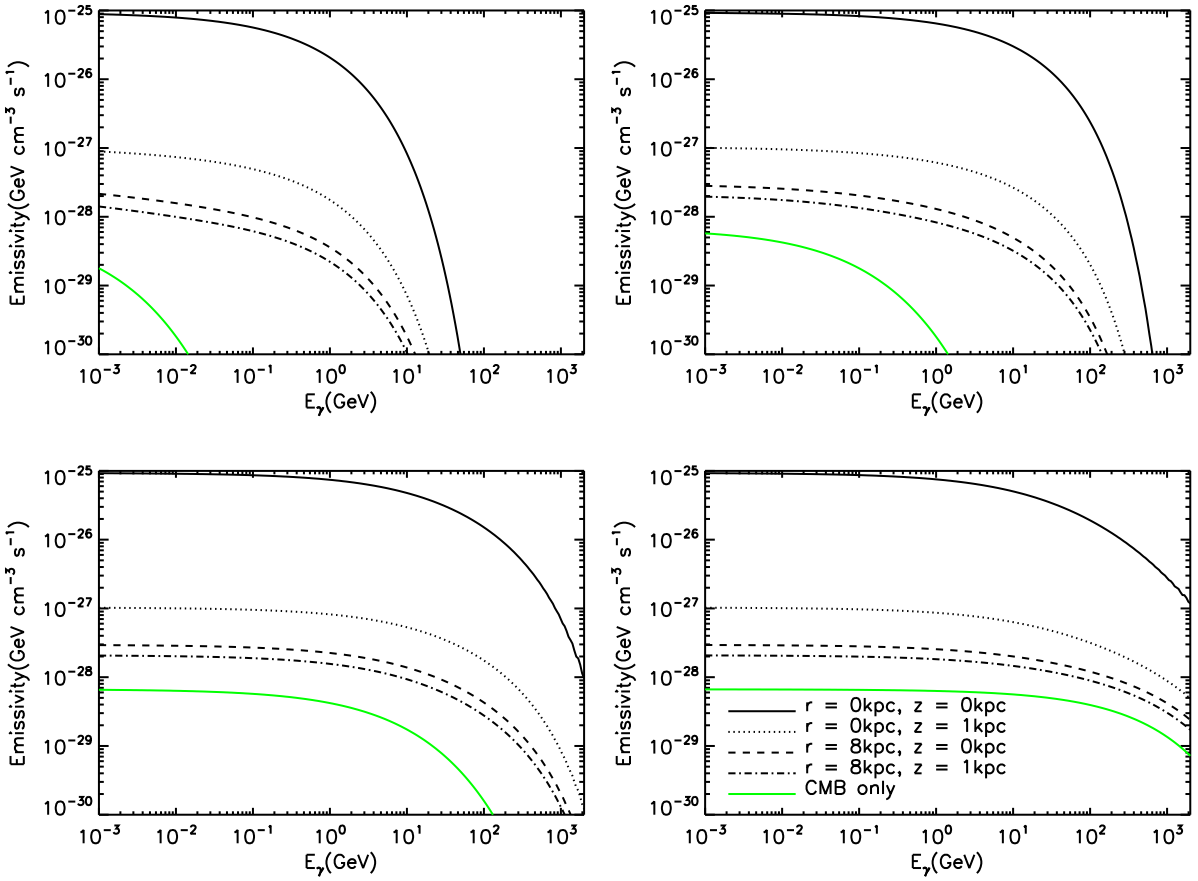

Figure 12. Gamma-ray IC emission spectrum for standard electron sources scattered by the diffuse ISRF in the MW plus the photons from the CMB, at each of the four reference positions of Fig. 6. The electrons have a power-law distribution $n(E) \sim E^{-3}$, with an exponential cut-off at $E_\mathrm{b} = 0.01$ TeV (top left), $E_\mathrm{b} = 0.1$ TeV (top right), $E_\mathrm{b} = 1$ TeV (bottom left) and $E_\mathrm{b} = 10$ TeV (bottom right). As a common reference to each panel, we also plot the IC spectrum resulting just from the CMB photon field.

All the IC SEDs are characterized by a break energy $E_{\gamma,\mathrm{b}}$, which is the energy at which a CR electron with the cut-off energy E_b would be scattered on the photons from the RFs at the peak of the SED, having energy $E_\mathrm{ph}^\mathrm{peak}$. This break energy appears as a knee in the IC SED and is proportional to $E_\mathrm{b}^2 \times E_\mathrm{ph}^\mathrm{peak}$. Thus, for the same RFs, the break energy will have lower values for low values of E_b and will increase with increasing E_b. This can be seen in Fig. 12, where the lowest values of $E_{\gamma,\mathrm{b}}$ are for $E_\mathrm{b} = 0.01$ TeV (top left panel), and the highest values of $E_{\gamma,\mathrm{b}}$ are for $E_\mathrm{b} = 10$ TeV (bottom right panel). One can also see that, for a given cut-off energy E_b, the break energy of the IC SED powered by the CMB is systematically lower than that of the IC SED powered by the ISRF, as expected due to the ISRF having a peak at higher energies than the CMB.

For energies beyond the break ($E_\gamma > E_{\gamma,\mathrm{b}}$), the IC SED is determined by the most energetic photons in the photon field, with the steepness of the SED depending on the colour of the RFs. Thus, the fall-off beyond the $E_{\gamma,\mathrm{b}}$ is steeper for the IC SED powered by the CMB than that powered by the ISRF, since, on the Wien side of the peak, the ISRF have a flatter spectrum than the CMB. One can also see from Fig. 12 that the flatter fall-off happens for the IC SED powered by the ISRF at (8,0) kpc, since there the RFs have the flattest SED (see Fig. 9).

For energies smaller than the break energy ($E_\gamma < E_{\gamma,\mathrm{b}}$), the IC SED is mainly determined by the CR electron spectrum. Thus, for a given cut-off energy of the electrons E_b, the IC SEDs have a similar shape, irrespective of the RFs powering the gamma-ray emission. This can be better seen in the bottom right panel of Fig. 12, where all the SEDs are below the break energy $E_{\gamma,\mathrm{b}}$ and therefore are parallel to each others. Another feature of the emission is that the IC flux from the ISRF seed fields always exceeds that from the CMB fields, even at large galactocentric radii where the energy density of the CMB exceeds that of the ISRF. This is because lower energy electrons are needed to produce a gamma ray of some fixed energy by IC scattering from the ISRF, and there are more such electrons available due to the prescribed power-law distribution in energy.

In Fig. 13 we show the IC SED, separated into components arising from the UV/optical and IR photons in the ISRF. Thus, for any position in the galaxy, one can see that for the lower energy cut-off of the electron spectrum, $E_\mathrm{b} = 0.01$ TeV (left-hand panel of Fig. 13), the break energy of the IC SED powered by the UV/optical RFs occurs at higher energies than that of the IC SED powered by IR RFs, which, in turn, occurs at higher energies than that of the IC SED powered by the CMB. At the higher energy cut-off of the electron spectrum, $E_\mathrm{b} = 10$ TeV (right-hand panel of Fig. 13), there is a crossover at high E_γ between the IC SED powered by UV/optical and IR RFs. This is because the cross-section for the IC scattering of UV/optical photons enters the Klein–Nishina relativistic regime before the IR photons.

Another interesting feature of these plots is that for the lower energy cut-off of the electron spectrum, the IC SEDs in the central regions of the disc have a break at larger gamma-ray energies than that of the IC SEDs from the outer disc. This is because the IC SED

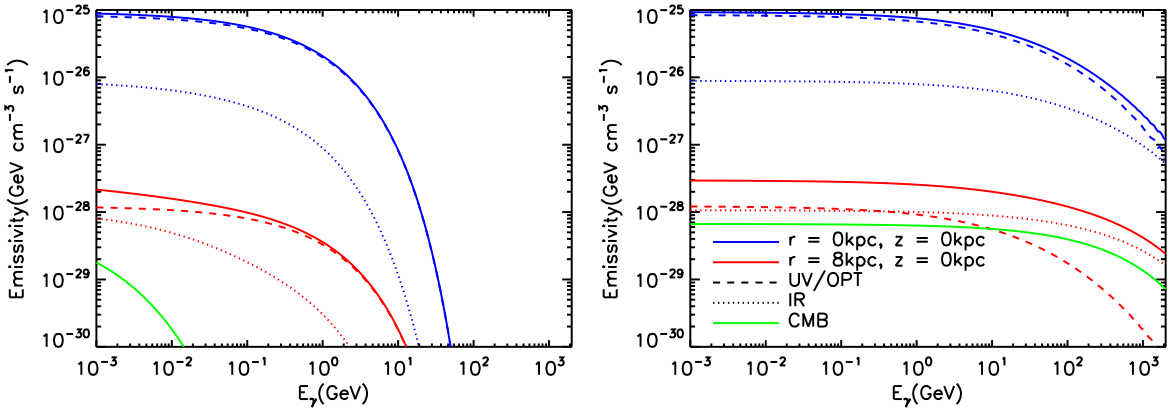

Figure 13. Same as in Fig. 12, but also showing the components of the IC SED due to IR photons (dotted line) and UV/optical photons (dashed line) from the ISRF. The plots are shown only for two reference positions in the plane of the disc and only for two cut-off energies, $E_b = 0.01$ TeV (left) and $E_b = 10$ TeV (right).

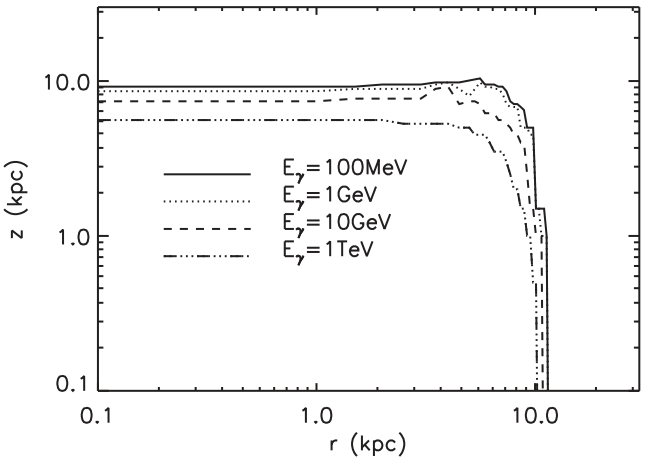

Figure 14. Contour plot showing the locus of positions at which the contribution from the CMB seed photons to the gamma-ray emission at a particular gamma-ray energy is equal to the contribution from diffuse ISRF photons. Contours are given in logarithmic steps of 10 in energy for 100 MeV, 1 GeV, 10 GeV, 100 GeV, 1 TeV and 10 TeV.

in the central regions is mainly powered by UV/optical ISRFs (see left-hand panel of Fig. 13), while the IC SED in the outer regions has approximately equal contributions from the UV/optical and IR RFs.

Overall, Figs 12 and 13 show that the IC SED powered by the ISRF dominates over the IC SED powered by the CMB, for all plotted positions. This dominance prevails within a ∼10 kpc radius sphere around the MW, as seen from the contour plots from Fig. 14. It should be noted that the radius of the sphere is expected to depend on the hardness of the CR electron energy spectrum. For CR electrons with a steeper spectrum than the fiducial power-law distribution $n(E) \sim E^{-3}$ that we have assumed, the ISRF component of IC emission will continue to dominate beyond 10 kpc, whereas for CR electrons with a flatter spectrum, the crossover point will be interior to 10 kpc.

6.2 Gamma-ray opacity

The same ISRF that dominate the production of IC radiation by CR electrons are also responsible for an attenuation of gamma rays. This attenuation arises through pair production resulting from interactions between the gamma rays and photons of the ISRF. The energy dependence of the pair-production cross-sections have been given by Gould & Schréder (1966). As a rough rule of thumb, the opacity to gamma rays of energy E_γ interacting with photons of wavelength λ peaks for $(E_\gamma/\mathrm{TeV})/(\lambda/\mu\mathrm{m}) \sim 1$, with a sharp cut-off towards shorter wavelengths. Thus, while the CMB controls the visibility of sources of gamma rays with E_γ around 1000 TeV, RFs in the range 0.1–100 μm control the visibility of sources in the 0.1–100 TeV range which is the typical energy range over which ground-based Cherenkov imaging telescopes such as HESS, Veritas, and in the future, CTA, operate. In the following, we show how the solution we have obtained for RFs in the MW in this wavelength range affect the visibility of galactic and extragalactic gamma-ray sources as a function of their galactic coordinates and (in the case of galactic sources) their distance from the Sun. The γ–γ opacity was calculated by performing the line-of-sight integral of the product of the ISRF energy density and the pair-production cross-section.

Fig. 15 shows the transmission curve (i.e. the fraction of photons reaching the Sun as a function of photon energy) for gamma-ray sources located at the Galactic Centre, and in the plane of the galaxy at a location 8 kpc from the Galactic Centre in the opposite direction to the Sun. Two main peaks in opacity are seen at ca. 2000 and 100 TeV, respectively, corresponding to the CMB and the FIR peak in the ISRF. The opacity peak associated with the CMB is deeper than that associated with the ISRF, since, though the energy density in the FIR is comparable to the 0.26 eV cm^{-3} of the CMB over the paths through the plane of the galaxy, the number density of the CMB photons is higher by about an order of magnitude. For the same reason, the UV/optical/NIR photons in the disc have a negligible effect on source visibility. The only exception is a ledge in the transmission curve from ca. 2 to 10 TeV, which is due to the line of sight passing through the intense radiation NIR fields produced by the bulge in the region of the Galactic Centre. As might be expected due to the cylindrical symmetry of the calculation of the ISRF, the visibility of the source at the Galactic Centre is, at all energies, higher by a constant factor corresponding to a factor of 2 in optical depth, compared to the source 8 kpc beyond the Galactic Centre.

An interesting feature of the plots is that already at energies of 50 TeV, a significant reduction of visibility of sources at the Galactic Centre is expected. This is physically attributable to the predicted sharp upturn in radiation energy density at 20 μm (see – top left panel of Fig. 8) from diffuse dust in the disc in the vicinity of the

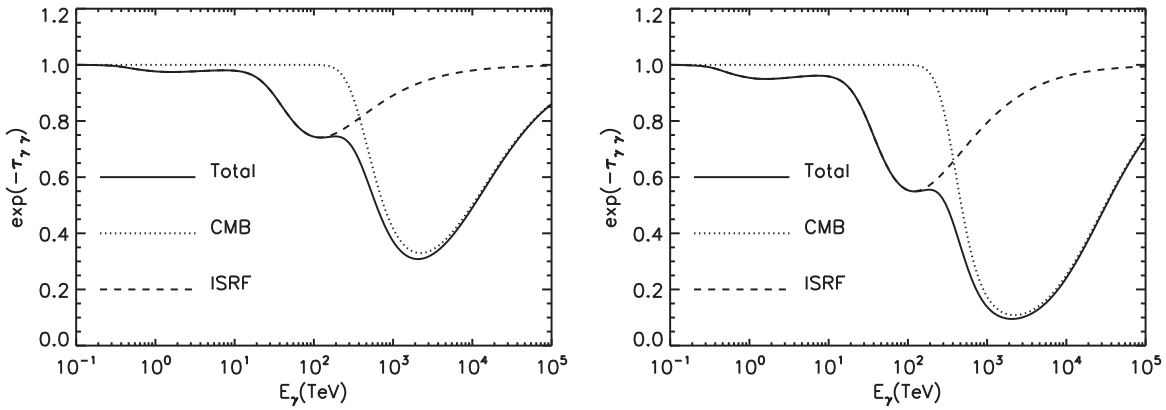

Figure 15. The transmission curve (i.e. the fraction of photons reaching the Sun as a function of photon energy) for gamma-ray sources located at the Galactic Centre (left), and in the plane of the galaxy at a location 8 kpc from the Galactic Centre in the opposite direction to the Sun (right). The Sun is assumed to be located at $R_\odot = 8$ kpc and $z_\odot = 0$ kpc. Both the contribution from the CMB and the ISRF are shown in the figure.

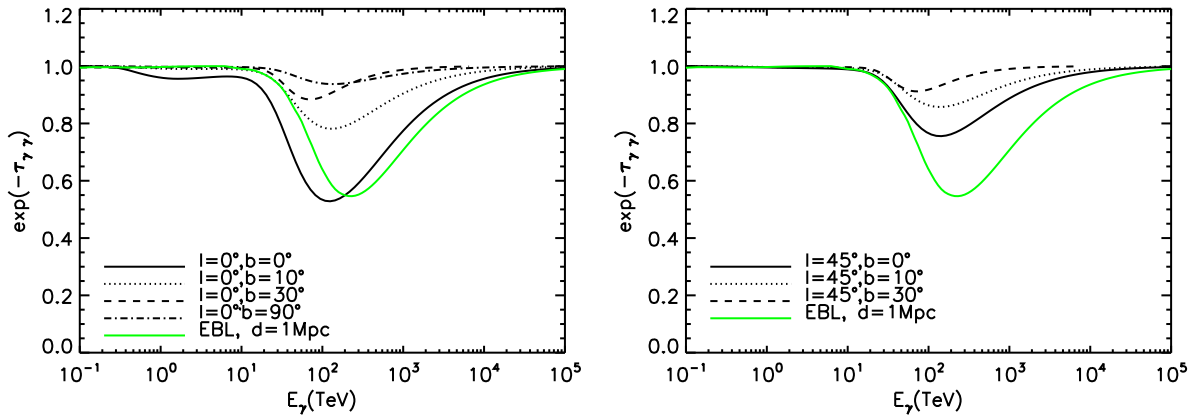

Figure 16. Left: the transmission curve for gamma-ray extragalactic sources located at galactic coordinates: ($l = 0°$, $b = 0°$) – solid line, ($l = 0°$, $b = 10°$) – dotted line, ($l = 0°$, $b = 30°$) – dashed line and ($l = 0°$, $b = 90°$) – dash–dotted line. Right: the transmission curve for gamma-ray extragalactic sources located at galactic coordinates: ($l = 45°$, $b = 0°$) – solid line, ($l = 45°$, $b = 10°$) – dotted line and ($l = 45°$, $b = 30°$) – dashed line. For these curves, only the opacity due to pair production resulting from interactions between gamma rays and photons of the ISRF in the MW is considered. The contribution due to the CMB and EBL is not included, as this would depend on the distance to the extragalactic sources. For comparison, the green curves show the effect on the transmission due only to the EBL light for a source located at a fiducial distance of 1 Mpc.

Galactic Centre heated by optical photons from the inner cusp of the bulge close to the Galactic Centre. This illustrates that even small efficiencies of conversion of optical to IR photons through absorption by dust can have a disproportionately strong effect on the pair-production opacity of gamma rays. The extreme steepness of the decrease in transparency between 20 and 100 TeV is due to a combination of two factors: First, the pair-production opacity is due to photons on the Wien side of the FIR dust emission peak, so that progressing to slightly higher gamma-ray energies brings a relatively large increment in energy density of longer wavelength IR photons into play. And secondly, this effect is compounded by the even larger number densities of the longer wavelength IR photons involved. We note that, since the IR RFs on the Wien side of the dust emission spectrum have a strong component of locally heated dust, the depth and steepness of the transmission curve between 20 and 100 TeV is dependent on the presence and amount of dust in the inner few tens of parsecs of the disc of the MW. This makes the visibility of pevatrons at, or seen through the Galactic Centre very dependent on complex physical processes controlling dust abundance in this region.

To examine the implications of our solution for the ISRF for the visibility of extragalactic sources, we have plotted in Fig. 16 transmission curves for external sources at selected galactic coordinates. To isolate the effect of the ISRF, these curves do not take into account the attenuation due to the CMB or the extragalactic background (EBL). For the purpose of comparison, a further transmission curve showing the pair-production absorption due to the EBL alone is plotted for a source located at a fiducial distance of 1 Mpc. For this, we used the EBL derived by Franceschini, Rodighiero & Vaccari (2008). As expected, the position of the peak in absorption due to the EBL is at higher gamma-ray energies than that due to the ISRF of the MW. This is because the SED of the EBL peaks at longer submm wavelengths, due to the EBL light being dominated by emission from cosmologically distant dusty sources. Nevertheless, even in the energy range up to 100 TeV, the effect of the ISRF on source visibility only approaches that of the EBL for sources in the Local Group (at distances scales of ca. 1Mpc) at low galactic latitudes. In the 0.1–20 TeV energy range, in which extragalactic sources have been commonly measured, the attenuation due to the ISRF is negligible, except for lines of sight into the inner galaxy, which in any case are avoided for extragalactic studies. A contour map in galactic coordinates of the 40 TeV opacity towards extragalactic sources due to pair-production ISRF is given in Fig. 17. We note that on this plot the contours are perfectly symmetrical

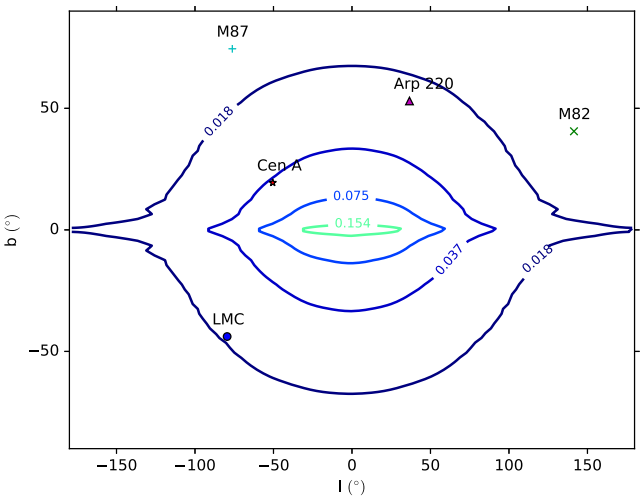

Figure 17. Contours of opacity at 40 TeV due to pair production in the predicted ISRF of the MW for extragalactic sources as a function of Galactic longitude l and latitude b. The positions of prominent nearby VHE sources are given on the plot.

between North and South, as we have taken the Sun to be located exactly in the plane of the MW. In reality, the Sun is displaced about ca. 15–20 pc North of the plane (e.g. Cohen 1995; Reed 2006; Joshi 2007), so the Northern sky will, at a certain level, be more transparent than the Southern sky. However, this introduces an asymmetry only of the order of 1 per cent in the opacities between North and South.

7 INFLUENCE OF THE MODELLED ISRF ON PREDICTED VHE EMISSION FROM ACCELERATORS OF CR ELECTRONS

IC scattering by CR electrons of either ISRF or CMB photons is generally not invoked to account for a major fraction of the VHE gamma-ray emission ($>\sim$1 TeV) from the diffuse ISM, due to the very high radiation losses of the electrons as they propagate away from their sources. For this reason we have considered only electron energy spectra with cut-offs of 1TeV and below when considering the IC emission from the diffuse ISM in Section 6.1. While the IC mechanism is commonly considered when accounting for the observed VHE emission in putative sources of CR, generally only scattering of CMB electrons has been considered. The reason for this is the predicted suppression of the scattering cross-section of ISRF photons compared to that for the CMB photons, due to the Klein–Nishina effect. Here, we show that in fact the ISRF has a strong effect on both the hardness and amplitude of the inferred energy distribution of CR electrons in sources in the galactic plane, especially within the solar circle.

This is illustrated by Fig. 18, which shows the predicted VHE IC emission from scattering of photons from the ISRF, compared to that from the CMB at different positions in the galaxy. The same electron spectrum with a power-law index of -3 as considered in Fig. 12 has been used for these predictions, but now with either no energy cut-off at all (RH panel) or with a cut-off at 1000 TeV (LH panel). As expected, the spectral slope of the emission from the ISRF steepens at high energy compared to that from the CMB. However, the curves for IC from the ISRF both with and without the cut-off in intrinsic electron energy spectrum only cross the curve for IC from the CMB at about 0.4, 30 and 300 TeV for sources in the plane situated at galactocentric radii of respectively 8, 4 and 0 kpc.

This shows that in general, the component of VHE IC emission from the ISRF will be important, and in many cases dominant, for sources within the solar circle. IC from the ISRF should therefore be considered when discussing leptonic hypotheses for the CRs giving rise to observed VHE gamma-ray emission from such sources. Most particularly, we note that, due to the Klein–Nischina effect, a harder energy spectrum of CR electrons will be inferred under this hypothesis compared to the case that only IC scattering off the CMB is considered, for sources located in the inner galaxy where the ISRF component dominates out to a few tens of TeV in photon energy. In general, this hardening will have to be considered, on a source-by-source basis, in conjunction with independent considerations influencing the hardness of the energy spectrum of electrons in the sources, when evaluating the leptonic hypothesis. This includes consideration of the predicted intrinsic hardness of the electron energy spectrum at injection for putative acceleration mechanisms, and/or the effect of radiation losses in the sources from the combination of synchrotron and IC losses.

8 SUMMARY

We use the formalism of the radiation transfer model of Popescu et al. (2011) and a new methodology that deals with the inner view of a galaxy and with the lack of direct observational constraints in

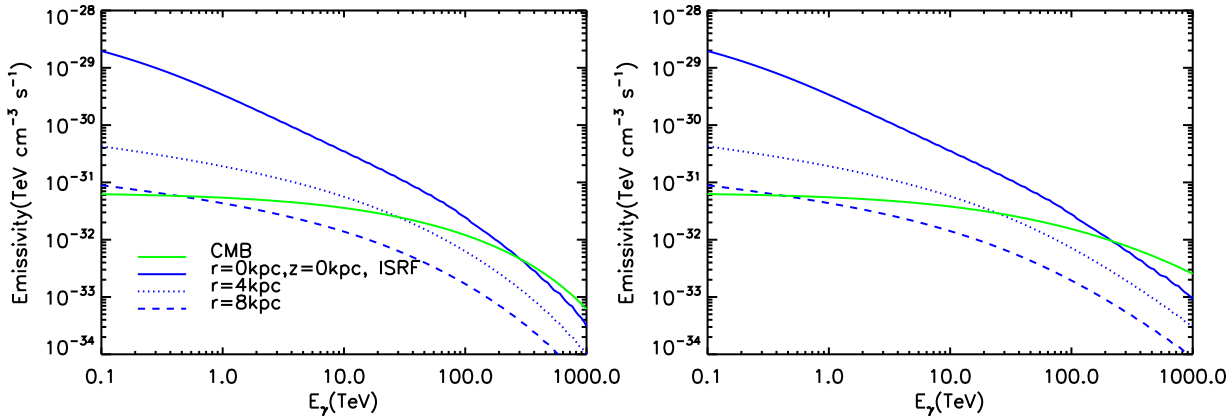

Figure 18. Predicted VHE IC emission from scattering of photons from the ISRF, compared to that from the CMB at different position in the galaxy. The electron spectrum has a power-law index of -3 and either an energy cut-off $E_b = 1000$ TeV (LH panel) or no cut-off energy(RH panel).

the UV–optical regime to derive an axisymmetric solution for the ISRF of the MW in direct and dust-re-radiated starlight, from 912 Å to 1 mm, over the volume within 24 kpc in galactocentric radius and ±10 kpc in height above the plane. The model of the MW was obtained by fitting the submm, FIR, MIR and NIR observed maps as seen from the position of the Sun.

The calculations were made using a modified version of the 2D ray-tracing RT code of Kylafis & Bahcall (1987), and the 3D ray-tracing RT code DART-RAY (Natale et al. 2014, 2015). Both codes include anisotropic scattering, and the dust model from Weingartner & Draine (2001) and Draine & Li (2007), incorporating a mixture of silicates, graphites and PAH molecules. The model for the dust emission incorporates a full calculation of the stochastic heating of small grains and PAH molecules. The geometrical model consists of a large-scale distribution of diffuse dust and stars, as well as of a clumpy component physically associated with the star-forming complexes. The large-scale distribution of stars consists of a thick and a thin stellar disc, a inner thin stellar disc and a bulge, all seen through a common distribution of dust. The diffuse dust is distributed into a thick and thin dust disc, respectively, on account of the different thickness of these structures.

We find that our model is able to account for the overall observed stellar and dust emission SED of the MW (as seen from the position of the Sun), as derived from *IRAS*, *COBE* and *Planck* maps at 1.2, 2.2, 3.5, 4.9, 24, 60, 100, 140, 240, 350, 550 and the 850μm. At 1.2 μm, the model underestimates the emission by 27 per cent, possibly indicating higher dust efficiencies in the submm than the WD01 model used in this paper or more complex geometries in the inner region due to the boxy-peanut shape of the bar/bulge structure. The agreement in the MIR, where the dust emission is predominantly powered by UV, means that the model prediction for the illumination of grains by UV light is good, both in the diffuse ISM and locally in the SF regions. This is the most direct constraint of the global distribution of UV light in the MW, where direct measurement of UV light can only be performed for nearby stars. The correct prediction of the colour between the peak of the SED in the FIR and the MIR shows that both the SFR and the probability of escape of non-ionizing UV light from SF regions in the diffuse ISM are also correctly modelled. Our model of the MW is thereby the first to consider all accessible emission components in a self-consistent radiation transfer treatment embodying absorption, anisotropic scattering and non-equilibrium emission from transiently heated grains, as well as local absorption from star-forming regions.

Comparison with the previously frequently used model GALPROP shows that the RFs calculated by GALPROP systematically differ from those predicted by our model. We ascribe the differences to the fact that GALPROP was not optimized to fit the all-sky multiwavelength images.

We describe and account for the spatial and spectral variations in the derived ISRF as a function of galactocentric position, and explore the imprint of these variations on the amplitude and spectrum of the component of gamma-ray emission due to IC emission from diffusely distributed CR electrons in the energy range from 1 MeV to TeV energies, using canonical reference spectra of electrons with a variety of cut-off energies. In general, IC from the UV–FIR component of the ISRF dominates IC from the CMB for IC emission over the volume out to galactocentric radii of around 10 kpc, and up to heights of 10 kpc, with only a moderate energy dependence of this volume of influence on the energy of the gamma rays. We also show that the FIR component of the ISRF, as predicted by our model, can strongly influence the derived amplitude and slope of the VHE IC emission above 1 TeV photon energy from discrete sources of CR electrons, compared to solutions only considering the component of IC from the CMB. This is despite the suppression of the cross-section for IC scattering of the ISRF at high energy due to the Klein–Nishina effect. Finally, we compute the pair-production opacity at VHE energies up to 100 TeV for gamma rays from sources located at various positions in our galaxy, as well as for extragalactic sources, giving a map of variation of opacity over the sky for the latter at a photon energy of 40 TeV.

The solutions for the UV/optical/FIR/submm RFs are available in electronic format for use in the analysis of gamma-ray emission in our Galaxy. To understand how they can be used, we need to draw attention to the main limitations and applicability of our model, as detailed in Section 4.3. First of all this paper presents the axisymmetric solution for the RFs of a MW having a WD01 dust type. If the submm grain efficiencies were higher than the predictions of the WD01 model, then this would be equivalent to an overestimation of the optical depth of the galaxy for a model that assumes a WD01 dust model. Because of the way our model was constructed, the solutions in the UV/optical (*B*, *V*, *I*) and MIR/FIR/submm are relatively robust against the choice of dust model, but the NIR solutions could be strongly altered should the dust model be different.

Because of the axial symmetry, the model presented in this paper cannot predict the variations in the diffuse ISRF between the arm and inter-arm regions, nor the variations due to the boxy-peanut shape of the bulge/bar structure in the inner disc. From the point of view of gamma-ray astronomy, this means that whereas the model can be used to predict the IC emission from the general population of CR interacting with the ISRF, it can only be used to place lower limits to the component of IC of any localized sources of CR geometrically associated with star-forming regions. In future work, we will use our 3D code DART-RAY to address this problem and to provide non-axisymmetric solutions for the RFs in the MW.

We also draw attention here to the fact that our model does not include any component of ISRF from a possible large-scale emission component from a galactic halo. If such a halo would be shown to exist, it would increase the predictions for the pair-production opacity of VHE gamma rays beyond the predictions given in this paper.

ACKNOWLEDGEMENTS

We would like to thank an anonymous referee for a very useful and constructive report which helped improve the paper. Cristina C Popescu and Giovanni Natale acknowledge support from the Leverhulme Trust Research Project Grant RPG-2013-418. The development of the RT code DART-RAY was supported by a previous grant from the UK Science and Technology Facilities Council (STFC; grant ST/J001341/1).

This research has made use of the NASA/IPAC Infrared Science Archive, which is operated by the Jet Propulsion Laboratory, California Institute of Technology, under contract with the National Aeronautics and Space Administration. The research has also made use of the Centre d'Analyse de Données Etendues (CADE; Analysis Center for extended data). *Planck* data have been used in this paper. *Planck* (http://www.esa.int/Planck) is a project of the European Space Agency (ESA) with instruments provided by two scientific consortia funded by ESA member states (in particular the lead countries France and Italy), with contributions from NASA (USA) and telescope reflectors provided by a collaboration between ESA and a scientific consortium led and funded by Denmark.

We acknowledge use of data on the RFs from GALPROP (http://galprop.stanford.edu). GALPROP development is supported through NASA grants and by the Max Planck Society.

REFERENCES

Ade P. A. R. et al., 2014, A&A, 571, 8
Adriani O. et al., 2011, Phys. Rev. Lett. 106, 1101
Aharonian F. A., Atoyan A. M., 2000, A&A, 362, 937
Baes M. et al., 2010, A&A, 518, 39
Bianchi S., 2007, A&A, 471, 7
Bianchi S., Xilouris E. M., 2011, A&A, 531, 1
Bienayme O., Robin A. C., Creze M., 1987, A&A, 180, 94
Cohen M., 1993, AJ, 105, 1860
Cohen M., 1994, AJ, 107, 582
Cohen M., 1995, ApJ, 444, 874
Davies J. I., Trewhella M., Jones H., Lisk C., Madden A., Moss J., 1997, MNRAS, 288, 679
Davies L. J. M. et al., 2016, MNRAS, 461, 458
De Looze I., Baes M., Fritz J., Verstappen J., 2012a, MNRAS, 419, 895
De Looze I. et al., 2012b, MNRAS, 427, 2797
De Looze I. et al., 2014, A&A, 571, A69
Devour B. M., Bell E. F., 2016, MNRAS, 459, 2054
Draine B. T., Li A., 2007, ApJ, 657, 810
Drimmel R., 2000, A&A, 358, L13
Drimmel R., Spergel D. N., 2001, ApJ, 556, 181
Driver S. P., Popescu C. C., Tuffs R. J., Liske J., Graham A. W., Allen P. D., de Propris R., 2007, MNRAS, 379, 1022
Driver S. P., Popescu C. C., Tuffs R. J., Graham A. W., Liske J., Baldry I., 2008, ApJ, 678, L101
Driver S. P. et al., 2012, MNRAS, 427, 3244
Franceschini A., Rodighiero G., Vaccari M., 2008, A&A, 487, 837
Girardi L., Groenewegen M. A. T., Hatziminaoglou E., da Costa L., 2005, A&A, 436, 895
Gould R. J., Schréder G., 1966, Phys. Rev. Lett. 16, 252
Graham A. W., Worley C. C., 2008, MNRAS, 388, 1708
Grootes M. et al., 2013a, ApJ, 766, 59
Grootes M., Tuffs R. J., Popescu C. C. Robotham A. S. G., Seibert M., Kelvin L. S., 2013b, MNRAS, 437, 3883
Gunawardhana M. L. P. et al., 2011, MNRAS, 415, 1647
Henry R. C., Anderson R. C., Fastie W. G., 1980, ApJ, 239, 859
Joshi Y. C., 2007, MNRAS, 378, 768
Kelvin L. S. et al., 2012, MNRAS, 421, 1007
Kelvin L. S. et al., 2014, MNRAS, 439, 1245
Khangulyan D., Aharonian F. A., Kelner S. R., 2014, ApJ, 783, 100
Kylafis N. D., Bahcall J. N., 1987, ApJ, 317, 637
Lee D. Baes M., Seon K.-I., Camps P., Verstocken S., Han W., 2016, MNRAS, 463, 2912
MacLachlan J. M., Matthews L. D., Wood K., Gallagher J. S., 2011, ApJ, 741, 6
Masters K. et al., 2010, MNRAS, 404, 792
Mathis S., Metzer P. G., Panagia N., 1983, A&A, 128, 212
Misiriotis A., Popescu C. C., Tuffs R. J., Kylafis N. D., 2001, A&A, 372, 775
Misiriotis A., Xilouris E. M., Papamastorakis J., Boumis P., Goudis C. D., 2006, A&A, 459, 113 (M06)
Miville-Deschênes M.-A., Lagache G., 2005, ApJS 157, 302
Moskalenko I. V., Strong A. W., 2000, 528, 357
Moskalenko I. V., Strong A. W., Ormes J. F., Potgieter M. S., 2002, ApJ, 565, 280
Moskalenko I. V., Porter T. A., Strong A. W., 2006, ApJ, 640, 155
Natale G., Popescu C. C., Tuffs R. J., Semionov D., 2014, MNRAS, 438, 3137
Natale G., Popescu C. C., Tuffs R. J., Debattista V. P., Fischera J., Grootes M. W., 2015, MNRAS, 449, 243
Pastrav B. A., Popescu C. C., Tuffs R. J., Sansom A. E., 2013a, A&A, 553, 80
Pastrav B. A., Popescu C. C., Tuffs R. J., Sansom A. E., 2013b, A&A, 557, 137
Planck Collaboration VIII, 2016, A&A, 594, 8
Planck Collaboration XXIX, 2014, A&A, 586, A132
Popescu C. C., Tuffs R. J., 2003, A&A, 410, L21
Popescu C. C., Tuffs R. J., 2013, MNRAS, 436, 1302
Popescu C. C., Misiriotis A., Kylafis N. D., Tuffs R. J., Fischera J., 2000a, A&A, 362, 138
Popescu C. C., Tuffs R J., Fischera J., Völk H., 2000b, A&A, 354, 480
Popescu C. C., Tuffs R. J., Kylafis N. D., Madore B. F., 2004, A&A, 414, 45
Popescu C. C., Tuffs R. J., Dopita M. A. Fischera J., Kylafis N. D., Madore B. F., 2011, A&A, 527, A109 (PT11)
Porter T. A., 2016, Contributed talk at the International Symposium on High-Energy Gamma-Ray Astronomy, 2016, July 11–15, Heidelberg, Germany
Porter T. A., Moskalenko I. V., Strong A. W., 2006, ApJ, 648, L29
Porter T. A., Moskalenko I. V., Strong A. W., Orlando E., Bouchet L., 2008, ApJ, 682, 400
Reed B. C., 2006, J. R. Astron. Soc. Can., 100, 146
Robin A., Creze M., 1986, A&A, 157, 71
Robin A. C., Haywood M., Creze M., Ojha D. K., Bienayme O., 1996, A&A, 305, 125
Robin A. C., Reylé C., Derriere S., Picaud S., 2003, A&A, 409, 523
Robitaille T. P., Churchwell E., Benjamin R. A., Whitney B. A., Wood K., Babler B. L., Meade M. R., 2012, A&A, 545, 39
Sodroski T. J., Odegard N., Arendt R. G., Dwek E., Weiland J. L., Hauser M. G., Kelsall T., 1997, ApJ, 480, 173
Strong A. W., Moskalenko I. V., Reimer O., 2000, ApJ, 537, 763
Tuffs R. J., Popescu C. C., Völk H. J., Kylafis N. D., Dopita M. A., 2004, A&A, 419, 821
Vulcani B. et al., 2014, MNRAS, 441, 1340
Wainscoat R. J., Cohen M., Volk K., Walker H. J., Schwartz D. E., 1992, ApJS, 83, 111
Weingartner J. C., Draine B. T., 2001, ApJ, 548, 296
Witt A. N., Johnson M. W., 1973, ApJ, 181, 363
Xilouris E. M., Byun Y. I., Kylafis N. D., Paleologou E. V., Papamastorakis J., 1999, A&A, 344, 868

This paper has been typeset from a TEX/LATEX file prepared by the author.